An Additively-Manufactured Molten Salt-to-Supercritical Carbon Di-oxide Primary Heat Exchanger For Solar Thermal Power Generation – Design And Techno-Economic Performance

Ines-Noelly Tano[1], Erfan Rasouli[2], Tracey Ziev[3], Ziheng Wu[4], Nick Lamprinakos[4], Junwon Seo[4], Lukas Balhorn[6], Parth Vaishnav[5], Anthony Rollett[4], Vinod Narayanan[1,2*]

1- *Department of Mechanical and Aerospace Engineering, 2132 Bainer Hall, University of California, Davis, CA 95616, USA*
2- *Western Cooling Efficiency Center, 215 Sage Street, Suite 100, University of California, Davis CA 95616, USA*
3- *Graduate student, Department of Engineering and Public Policy, Carnegie Mellon University, 5000 Forbes Avenue, Pittsburgh, PA, 15213, USA*
4- *Department of Material Science and Engineering, Carnegie Mellon University, 5000 Forbes Avenue, Pittsburgh, PA, 15213, USA*
5- *School for Environment and Sustainability, University of Michigan, 440 Church Street, Ann Arbor, 48109, MI, USA*
6- *Visiting undergraduate scholar at UC Davis from RWTH University, Aachen, Germany*

* *corresponding author; email: vnarayanan@ucdavis.edu*

ABSTRACT

The design and techno-economic performance of a compact additively manufactured (AM) molten salt-to-supercritical carbon di-oxide (sCO_2) primary heat exchanger (PHE) for solar thermal application is described. The PHE design consists of sCO_2 flow through an array of microscale pin fins while the MS flows through mm-scale rectangular channels. Constraints imposed by AM using laser powder bed fusion method are considered in the design. Structural and fluid flow simulations are performed to arrive at a viable design of the core and headers. A simplified one-dimensional steady state model for the PHE is developed including the impact of surface roughness from the AM process. A process-based cost model is used to determine the tradeoff between thermofluidic design and manufacturing cost.

A parametric study is performed using the thermo-fluidic and cost models to determine the set of geometrical and flow variables that result in high power density and low cost, while restricting the pressure drop on the sCO_2 side to less than 2% of line pressure. Flow rates of MS and sCO_2 were varied over heat capacity rate ratios ranging from 0.2 to 1. Results indicate that it is possible to design a low-pressure drop AM PHE with an effectiveness of 90% and a power density in excess of 10 MW/m^3 (including headers). Fabrication of representative nickel superalloy specimens are shown to demonstrate that low-porosity parts with the requisite dimensional tolerance of PHE core can be generated.

KEYWORDS

Molten salt, supercritical carbon di-oxide, heat exchanger, Additive manufacturing, process-based cost model, nickel superalloy

NOMENCLATURE

MS	Molten Salt
AM	Additively Manufactured/ Additive Manufacturing
CFD	Computational Fluid Dynamics
C	Heat capacity rate (W/K)
C_r	Heat capacity rate ratio (dimensionless)
c_p	Specific heat capacity (J/kg-K)
D	Diameter (mm)
f	Friction factor
F_{corr}	Calibration factor to account for actual flow configuration
H	Height (mm)
h	Convective heat transfer coefficient (W/m^2-K)
H282	Haynes 282 alloy
i	Specific enthalpy rate (W/kg)
k	Thermal conductivity (W/m-K)
L	Length (m)
LPBF	Laser Powder Bed Fusion
$\dot{m}$	Mass flow rate (kg/s)
MAD	Mean Average Deviation, see Eq. A.21
N	Number of channels or plates
NTU	Number of Transfer Units
Nu	Nusselt number
P	Pressure (Pa)
PBCM	Process-Based Cost Model

PCHE	Printed Circuit Heat Exchanger
PHE	Primary Heat Exchanger
Pr	Prandtl number
Q	Heat exchange rate over the PHE (kW)
$\dot{q}$	Heat transfer rate in control volume analysis (W)
Re	Reynolds number
Rz	Average peak-to-valley roughness
S	Transverse or longitudinal pitch in pin array; fin pitch on MS side
sCO_2	Supercritical carbon di-oxide
T	Temperature
Th	Thickness
UA	Overall heat transfer coefficient (W/m^2-K)
V	Velocity (m/s)
W	Width (mm)

SUBSCRIPTS

A_{min}	Minimum cross-sectional area in pin array
c	Cold
ch	Channels
ci	Cold inlet
co	Cold outlet
Counter	Counter-flow region
H	Hydraulic
h	Hot
hi	Hot inlet

ho	Hot outlet
in	Inlet
L	Longitudinal
min	Minimum
max	Maximum
out	Outlet
MS	Molten salt
pin	Pin
plate	Cold plate/pin array
sCO_2	Supercritical carbon di-oxide
T	Transverse
t	Total
th	Thermal
wall	Heat exchanger material

SYMBOLS

α_H	Aspect ratio of channel
β	Pitch ratio in pin array, ratio of transverse or longitudinal center to center distance to diameter
Δ	Differential
ε	Effectiveness of heat exchanger
μ	Dynamic viscosity (Pa-s)
η_o	Overall surface efficiency of finned surface
ρ	Density (kg/m^3)

INTRODUCTION

Concentrated solar power, when coupled with thermal storage, offers the opportunity to generate power during off-sun hours thereby making the technology dispatchable. The recent focus in solar thermal electric power generation has been on operating at higher receiver temperatures and using the supercritical carbon di-oxide (sCO_2) power cycle. The potential for thermal storage, as opposed to the more expensive battery storage of associated utility scale photovoltaic systems, is often touted as a key advantage of the solar thermal power generation route. Molten salt (MS) solar thermal systems, which permit sensible thermal storage, are being considered as a potential candidate, based on the industry's past experience with nitrate-based salts (Mehos et al., 2017). However, higher temperature salts, such as chloride salt mixtures are needed to obtain desired turbine inlet temperatures of 700 ^{o}C. As per the US Department of energy's Generation 3 technologies roadmap for concentrating solar power systems, the MS-to-sCO_2 primary heat exchanger (PHE), which transfers heat from the stored salt in the hot tank to the working fluid of the power generation cycle (sCO_2), is a key component that needs to be developed in order to facilitate the molten salt pathway to solar thermal power generation (Mehos et al., 2017). The operating conditions of this PHE are demanding – with surface temperatures of up to 720^{o}C on the MS side, pressure of 200 bar on the sCO_2 side, and potential for corrosion by the salt.

Three potential conceptual designs were identified for MS-sCO_2 PHE in the DOE report (Mehos et al., 2017)- a shell and tube design, a printed circuit heat exchanger (PCHE) design, and a shell and tube serpentine design. However, details of design, modeling and performance were not reported. A typical architecture for a compact metallic PHE for this application is that of microchannel (printed circuit/micro-lamination) heat exchangers. The key steps in the fabrication process include chemical etching of multiple metallic shims to create flow geometries and diffusion bonding/brazing a stack of shims to create a heat exchanger. Headers need to be designed and brazed or welded to the stack. Such heat exchangers have been proposed for recuperators in the sCO_2 cycle by many groups. Variants on the design include changes to the patterns etched in the shims that form channels such as straight, zig-zag channels or pin arrays (Pandey et al. (2020), Zhang et al. (2019), Saeed and Kim (2019), Jing et al. (2020), Wang et al. (2019), Khalesi and Sarunac (2019), Shi et al. (2020), Chu et al. (2019)). These studies have typically considered lower temperature applications for which the hot side inlet temperature is lower than 600 ^{o}C. These temperatures permit the use of stainless steel or Inconel for which etching and diffusion bonding schemes are well established.

Katz et al. (2021) experimentally studied a 17-plate photochemically etched and diffusion bonded 316/316L stainless steel PCHE with zigzag channels using Helium and sCO_2 at temperatures up to 580 °C and 350 °C, respectively. While the main objective was to investigate pressure drop and heat transfer at these temperatures in a commercially available configuration and develop correlations for fluids frequently used with PCHE, the work also provided some insight into the header contribution to the overall thermofluidic performance.

Shi et al. (2020) studied both numerically and experimentally an airfoil-rectangular microchannel photochemically made from stainless steel. In the numerical work, the hot side with the airfoil geometry, the $MgCl_2$-KCl salt temperature varied from 534 to 800 °C and the cold side had a straight rectangular microchannel geometry where sCO_2 flowed at temperatures between 506 and 800 °C. The results were compared to a previous experimental study (Wang et al. (2019)) from the same group using a ternary salt (Hitec) and a synthetic oil (YD-325) and lower temperatures (198 to 254 °C and 81.5 to 165.2 °C for the salt and oil, respectively). The study showed a maximum deviation of +/- 12% between experimental and numerical results and the performance evaluation criterion, defined as the heat transfer enhancement to pressure drop penalty ($(Nu/Nu_{PCHE})/(f/f_{PCHE})^{1/3}$), for this design was improved compared to a zigzag channel.

For the chloride MS-sCO_2 heat exchanger, given the higher inlet temperature and corrosion of molten salt, high temperature Ni superalloys are needed, for which etching and diffusion bonding schemes are still being developed. Some published work on tensile tests of diffusion bonded H230 specimens, with and without nickel plating, showed that failure at 750 °C occurred in the diffusion bonded regions. The yield strength was between 76% (with plating) and 82% (non-plated) of base metal strength (Kapoor et al. (2016). Diffusion bonding/brazing also restricts the PHE design choices to similar channel architectures on the hot and cold sides, thereby imposing a high pressure drop in the fluid with high heat transfer coefficient. This penalty occurs because the hot and cold layers need to be of the same dimension in order to maintain uniform stress across the diffusion bonded stack.

Caccia et al. (2018) demonstrated the viability of a ZrC/W cermet PCHE for sCO_2. In addition to a good corrosion resistance at 800 °C and 200 bar, the fabricated heat exchangers possessed a set of thermo-mechanical properties that allow the device to exhibit a high failure strength of over 350 MPa but also to have core power densities of

8-10 MWth/m^3. An effectiveness of 95 % for a heat exchanger comprised of straight semi-circular parallel channels was estimated.

In this paper, the mechanical and thermofluidic design of a compact additively manufactured (AM) chloride MS-sCO_2 primary heat exchanger is described. The use of AM techniques has become more prevalent in heat transfer and thermal management applications using macro- and micro-scale heat sinks (Snyder et al. (2015), Stimpson et al. (2016), Stimpson et al. (2017), Kirsch and Thole (2016), Kirsch and Thole (2017), Cormier et al. (2014), Dupuis et al. (2016), Ho et al. (2017), Ibrahim et al. (2017), Tsopanos et al. (2005)). A key advantage of AM compared to conventional fabrication techniques is that it offers an unprecedented level of versatility to the designs and reduce material waste typical in subtractive machining processes (Ngo et al. (2018)). Greiciunas et al. (2019) fabricated an inter-layer heat exchanger using selective laser melting (SLM). This heat exchanger consists of a stack of plates with slanted conduits that act as pins on one side and promote fluid mixing on the other by allowing different plates to communicate. The authors numerically demonstrated that this more efficient design reduced flow maldistribution and enhanced the performance of the heat exchanger. Comparing a zigzag PCHE against Gyroid and Schwarz-D structures for sCO_2 applications, Li et al. (2020) numerically showed that although the zigzag channel is typically a favorable configuration for heat transfer, the Gyroid and Schwarz-D geometries further enhance the Nusselt number due to the increased turbulent mixing and surface areas. Despite a larger pressure drop, the triply periodic minimal surface structures displayed a performance evaluation criterion that was 17-100% higher than that of the zigzag PCHE, with a more pronounced enhancement at lower Reynolds numbers. Ho et al. (2020) conducted an experimental study of two rhombi-octet porous lattice PHE fabricated through SLM. Using air and water it was showed that at the same porosity, the lattice with smaller unit size exhibited a lower thermal resistance. Ferster et al. (2017) experimentally evaluated the performance of triangles, stars, and dimpled-sphere arrays fabricated from direct metal laser sintering. The experiment was conducted with air flow for Reynolds number ranging from 300 to 30,000 and the results were compared against conventional cylindrical pin arrays. The geometry was found to have a greater impact on the performance than the spacing. The cylindrical pin and the triangle pin with point facing the flow achieved the highest heat transfer, followed by the dimple and the stars while the lowest pressure drop was that of the triangle with vertex facing the flow.

Literature on high temperature MS-sCO_2 PHE is scarce; with the exception of Caccia et al. (2018), all PHE designs are for lower temperature salts. While AM has been used for

heat exchanger and heat sink fabrication, literature on use of metal AM for high pressure and high temperature applications is extremely limited. The **objective** of this study is to present the design of a compact additively manufactured chloride MS-sCO_2 PHE for solar thermal applications using a laser powder bed fusion (LPBF) method. The design of the PHE is first described, including mechanical design of the core and headers. Feasibility of AM fabrication is demonstrated in two steps. First, fabrication of low-porosity H282 parts is demonstrated. Next, fabrication of sample pin arrays of the dimensions of the PHE using H282 is demonstrated. A simplified numerical model for thermal performance of the PHE is then developed with consideration of surface roughness from the AM process. The correlations used in the model are validated against detailed computational fluid dynamics (CFD) simulations of a unit strip of the core. The validated model is used in parametric studies to identify the impact of geometrical and process variables on the performance of the heat exchanger. A concurrent process-based cost model (PBCM) is used to assess the impact of varying these parameters on manufacturing cost of the PHE. The tradeoffs between performance and cost are discussed.

PHE DESIGN

The concept of the proposed PHE design is shown in Figure 1. As depicted in the cut-away view in Figure 1a and d, the core of the PHE is comprised of several "cold plates" within which sCO_2 flows through microscale pin arrays, while MS flows around and in between the plates in parallel channels. The PHE cold plates are connected to distributor and collector headers (Figure 1b, c and e). A staggered pin array architecture (see detail in Figure 1e and f) is used for the microscale regions since it lends to higher heat transfer rate and better flow distribution than parallel microchannels (Peles et al. (2005)). The sCO_2 headers are located on the top side of the duct and the sCO_2 stream enters through the inlet header and is distributed into plates as shown on Figure 1b. Within each plate, sCO_2 enters into a cross flow section, followed by a counter-flow section and a second cross flow region before the fluid exits the PHE (Figure 1e). Considering sCO_2 and molten salt flow directions, the sCO_2 entrance region is partially in a cross-flow configuration. Although fully counter-flow design is favorable for optimal heat exchange, since headers must be located outside the molten salt channel to avoid flow obstruction, existence of this cross-flow region is inevitable.

Straight fins are located on the MS side to enhance heat transfer area while facilitating ease of drainage by gravity (when oriented vertically) during idle conditions. The AM PHE design alleviates limitations imposed by the microlamination approach to designing the conventional PCHE by allowing for independent variations in aspect

and pitch ratio of the pin array on the sCO_2 side and for variations between the MS and sCO_2 flow passage designs. Furthermore, the headers can be directly integrated and printed with the core to reduce failure locations. Scale-up of the design can be achieved by increasing the number of sCO_2 plates in the core and proportionally increasing the header depth. Additional scale-up can be achieved through modularity, by connecting multiple such PHE units. A PHE of dimensions that could be fabricated in the available LPBF machine (EOS M290, with a build area of 25 cm x 25 cm) is discussed as a baseline.

The design of the PHE was divided into the core (pin array) and header sections. A key consideration in the design of the PHE is the large mechanical stresses imposed on the structure by the 200-bar pressure on the pin array by sCO_2. For each section, iterative mechanical integrity and CFD simulations was performed to ensure that the final design was structurally sound and able to withstand the imposed stresses, while optimizing the usage of fabrication material and demonstrating desirable flow uniformity. The mechanical integrity and CFD simulations of the PHE heat exchanger were performed using ANSYS Mechanical and Fluent, respectively.

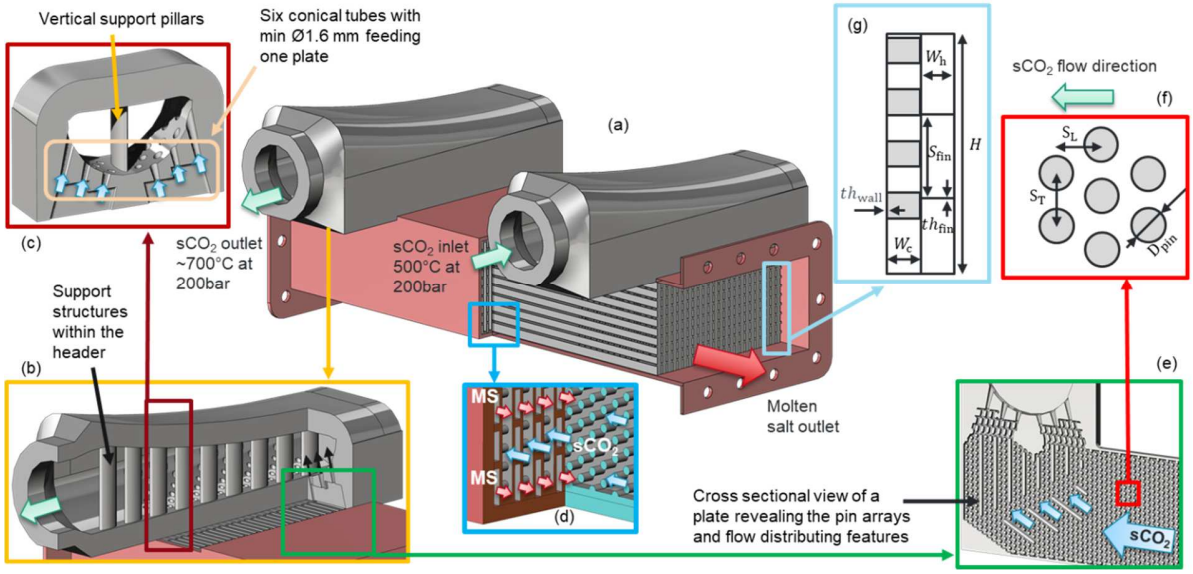

Figure 1. Proposed concept for AM PHE. (a) solid model of the PHE with a cut-away view of the core architecture; (b) PHE header cut-away showing support structures and passage of sCO_2 into pin array plates; (c) details of the header design with vertical support pillars and distributor tubes to direct flow into plates, (d) cut-away of the core showing sCO_2 and MS passages; (e) cut-away view of a cold plate revealing the pin arrays and distributing features; (f) top view schematic of the pin array; (g) schematic of the cross-sectional view of a cold plate and adjacent hot side.

The heat exchanger was designed to be additively manufactured with Haynes 282 powder. This alloy is composed of 57% Nickel, 20% Chromium, 10% Cobalt, 8.5%

Molybdenum and trace amounts of other elements. It also exhibits good resistance in oxidizing environments up to 1149°C and displays long-term thermal stability (Haynes International, 2020). For the PHE design, the maximum allowable stress target was set based on creep at 720 °C for a 100,000-hour lifetime for H282. For this time and temperature combination and based on a Larson and Miller (1952) approach for steady state creep, the stress for rupture is 151 MPa, while the stress to attain 1 % creep is 98 MPa (Haynes International, 2020).

Core design

Several important parameters play a role in determining the overall design of the PHE, including geometrical parameters of the core shown in Figure 1e and f such as the cold plate spacing, MS-side fin spacing, cold plate pin array design, and flow parameters such as hot and cold flow inlet temperatures, and mass flow rates. The stress distribution on an elemental repeating unit of the pin array was evaluated to minimize the maximum value of the von Mises equivalent stress dictated by the creep limit. A parametric study was performed in order to determine the shape of the pin that would yield the lowest stress. Various pin shapes (circular, elliptical, hourglass) were considered, with additional iterations on the pin height, wall thickness and fillet radii at the base of the pins. From the simulation results, it was observed that a circular cross-section for the pin associated with a hexagonal lattice of pins was the optimal combination to reduce the maximum stress in pin array unit cells. The final unit cell geometry, that defined the upper limit of transverse and longitudinal spacing, and the lower limit of wall thickness and pin diameter for the thermofluidic analysis, are summarized in Table 1.

Table 1. Dimensions of the final pin array unit cell design

D_{pin} (mm)	1.2
β_T	2.05
β_L	1.76
th_{wall} (mm)	0.5
H_{pin} (mm)	1.8
Fillet radii (mm)	0.8-0.4

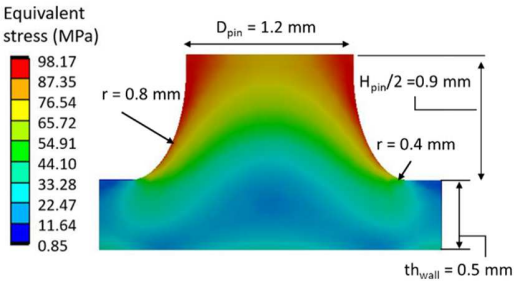

Header design and flow uniformity

The structural support features within the header to withstand 200 bar internal

pressure are shown in Figure 1b and in greater detail in Figure 1c. Periodically-located vertical pillars resulted in peak stress of 110 MPa in the pillars. Upon completion of the mechanical design, CFD simulations were performed on the header to characterize the flow distribution into the pin array plates from the header. The fluid body within the structurally designed header is shown in Figure 2a where the connection between header and each of 26 plates can be distinguished. Flow was directed into each plate from the header via six conical tubes, see Figure 1c. The fluid body was meshed and simulated in Ansys Fluent using k-epsilon turbulence model for baseline flow rate of 50 g/s. A porous media model was imposed on the region called out in red in Figure 2a to take into account the effect of pressure drop across the pin array on the flow distribution in the header. The porosity parameters for viscous and inertial terms were obtained based on pressure drop through pin array obtained by simulating a narrow strip of the core for the range of relevant flow rates. The mass flow rates discharged into each of 26 plates are plotted in Figure 2b for 50 g/s overall incoming sCO_2 flow rate entering the header (baseline flow rate in parametric study). The mass flow rate into each plate varied between 1.90 g/s and 1.93 g/s with the Mean Absolute Deviation (MAD, second ordinate in Figure 2b) among plates relative to the average of less than 1%. The low MAD indicates a viable header design for the PHE, which while intricate, can readily be fabricated using AM.

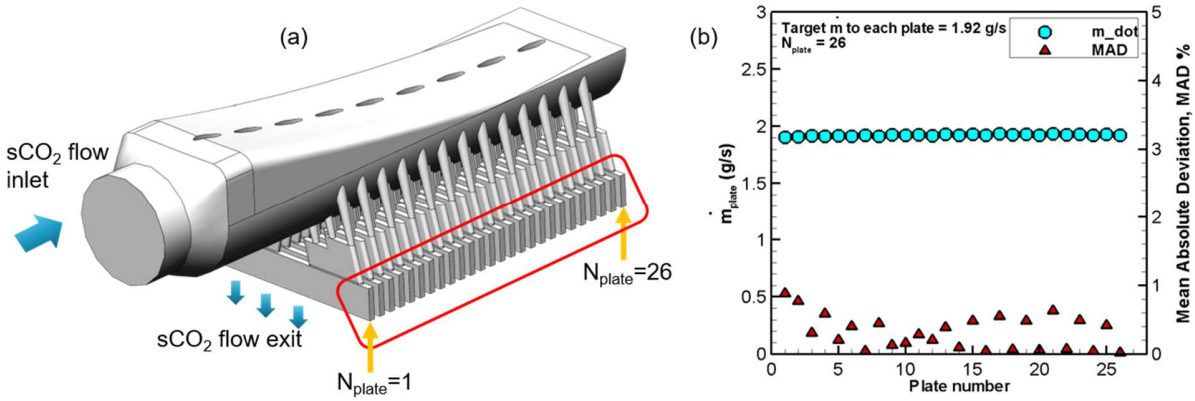

Figure 2. (a) View of the fluid body within the header (b) Distributed sCO_2 flow rate into each plate

The next step in the design was to ensure uniform flow distribution in the counter-flow region within each sCO_2 pin array plate. By virtue of symmetry, the computational domain consisted of pin array and molten salt channels with one-half thickness, as shown in Figure 3. In the meshing module of ANSYS, the flow domain was discretized using the method of proximity and curvature, and the near wall region was refined on both the sCO_2 and molten salt sides with inflation layers. Since the Reynolds number (Re) for the sCO_2 side was 1400, a k-ω SST turbulence model was

selected for better treatment of flow separation in the wake of the pins. Prior work in literature has shown that the flow in such pin arrays transitions to turbulence at a Re of 150 (Rasouli et al. (2017)). The MS side was modeled as a laminar flow since the Re was about 30. Symmetry boundary conditions were defined as shown in Figure 3. The inlet and outlet sCO_2 faces were defined as mass flow inlet and pressure outlet, respectively. Analogous boundary conditions were applied on the side faces for the inlet and outlet faces for the salt. All other external faces (top, bottom, sides) were defined as adiabatic. Temperature dependency of the molten salt, sCO_2 and H282 properties over a range from 500 °C to 800 °C were used in the simulations. Convergence for simulations was deemed achieved when the residuals for energy, velocity, dissipation, and turbulent kinetic energy attained values of 10^{-8}, 10^{-4}, 10^{-4}, and 10^{-3}, respectively. The mass imbalance between the inlet and exit at convergence was 5.2 $*10^{-3}$ percent.

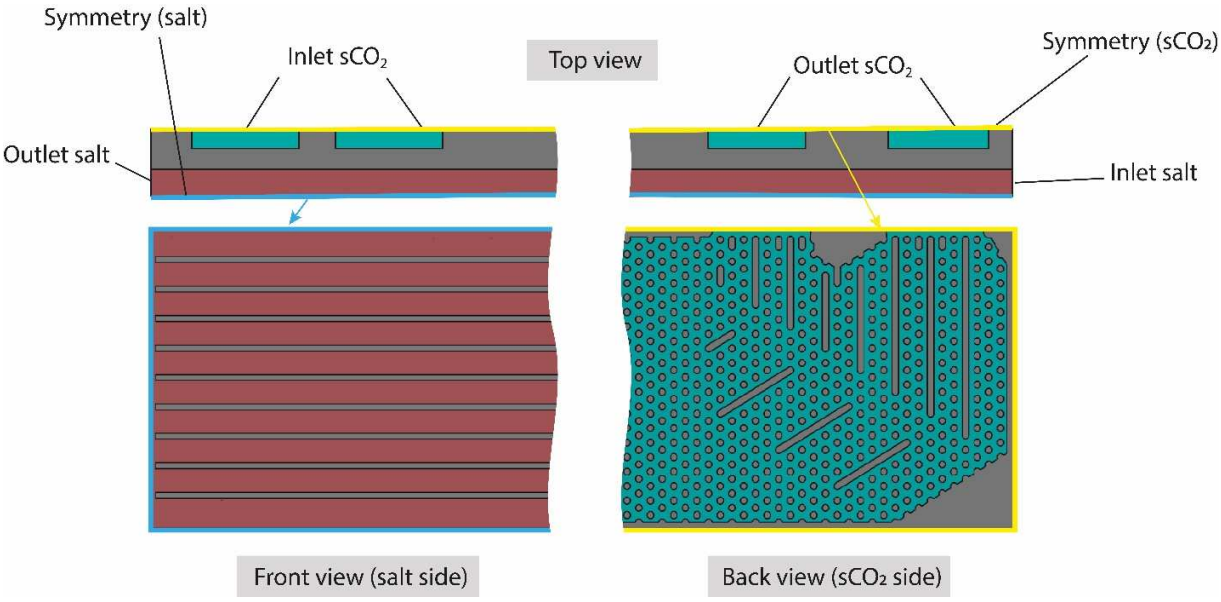

Figure 3. Schematic of the heat exchanger plate with one-half thickness including solid and fluid domains.

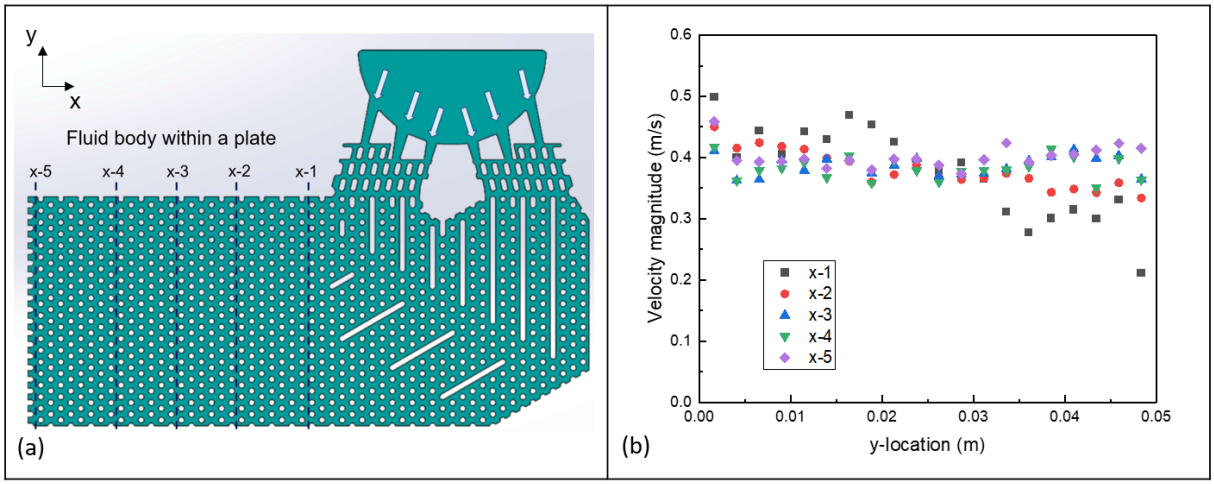

Figure 4. (a) Fluid body within the plate b) Velocity magnitude along the y-direction at different x-location in the plate.

A grid independence study with meshes varying from 15 to 21 million nodes was performed to ensure sufficient resolution to provide invariant results. The parameters altered to obtain the different meshes were the element proximity minimum size as well as the number of inflation layers. Between 15 and 21 million nodes meshes, the proximity and curvature minimum size varied from 0.15 mm to 0.122 mm and the number of inflation layers varied from 10 to 12 on the sCO_2 side and 7 to 10 on the molten salt side. A difference of less than 1 % in pressure drop on the cold side and less than 0.1 % in exit temperatures was noted from one mesh size to the next above 17 million nodes. Results from the 17 million nodes simulation are therefore used for analysis and post-processing.

To quantify the flow uniformity on the sCO_2 side, velocity magnitude along the height of the plate (y-direction) at five different locations along the flow direction (x-direction) are plotted as shown in Figure 4b. The velocity magnitudes are seen to be reasonably close to one another and the largest deviation observed is at location x-1 due to its proximity to the cross flow section and the inlet of the flow domain. The mean average error of velocity magnitude at location x-1 is 16 % but the average MAD at locations x-3 to x-5 is only 3.6 %, indicating adequate flow uniformity across the height of the pin array in a majority of the counter-flow section.

PHE Additive Manufacturing Considerations

The design of the heat exchanger is dictated by AM constraints with an emphasis on avoiding large-scale overhanging features, i.e., a structure built directly on a powder bed without being anchored to a solid substrate. An important consideration in the design of an AM PHE was to ensure that the AM process was able to generate high

density, pore-free parts. Fabrication runs were performed in an EOS M290 LPBF machine with gas atomized H282 powder to determine the process window at a pre-heat of 200°C to produce pore-free builds. Once the process window was identified, small-scale specimens, representative of the core geometry were fabricated to determine the dimensional tolerance that could be achieved.

Porosity control is often the first optimization task when a non-standard alloy is used in AM since low porosity is a critical factor for avoiding premature failure in the additively built PHE. The essential idea of porosity control is to optimize the laser parameters by varying the laser power, speed, and hatch spacing so that the resulted melt pool can 1) ensure sufficient overlaps to fully melt the prescribed volume of the components and 2) maintain a stable morphology to avoid the formation of keyhole porosity which is induced by the collapse of a metal vapor cavity. Ensuring high part densities may limit the build rate, which is directly controlled by the selection of laser speed, hatch spacing, and layer thickness. Therefore, there is a tradeoff between low porosity and low cost, which is usually achieved by maximizing build rate. Table 2 summarizes the three laser parametric candidates within the process window and their corresponding part densities measured using the metallurgical cross-sectioning method. The higher build rate did sacrifice a little part density as the laser speed increased from 959 mm/s to 1772 mm/s when switching from S#1 to S#3, almost doubling the build rate. Yet, all three parameter sets achieved more than 99.9% in part density. Note that the EOS M290 machine has a maximum laser power of 370 W which limited the maximum applicable laser speed (and lowest part cost) with the concern of lack-of-fusion. That said, the build rate can potentially be further improved if a higher power laser is available in a more advanced LPBF system.

Table 2. Part densities and plate surface roughness resulting from three optimized laser parametric candidates, selected to assist the design and development of the additively built PHE using H282 gas atomized powder in an EOS M290 LPBF system.

Parameter label	Power (W)	Velocity (mm/s)	Hatch Spacing (mm)	Energy density (J/mm^3)	Density (%)	Roughness R_z (µm)
S#1	250	959	0.11	59.25	99.99	129.05
S#2	350	1366	0.11	58.23	99.96	102.06
S#3	370	1772	0.11	47.46	99.92	186.61

Table 3. Measured pin dimensions of micro pin array fabricated using three optimized sets of laser parameters in an EOS M290 LPBF system.

Pin diameter	Printing parameters	Measured pin dimension	Percentage deviation from the design	Measured pin dimension	Percentage deviation from the design

(mm)		along x (mm)	along x	along y (mm)	along y
1.2	S#1: 250 W & 959 mm/s	1.310 ± 0.074	9.17% ± 6.2%	1.255 ± 0.066	4.56% ± 5.5%
	S#2: 350 W & 1366 mm/s	1.376 ± 0.079	14.68% ± 6.5%	1.226± 0.049	2.15% ± 4.1%
	S#3: 370 W & 1772 mm/s	1.327 ± 0.083	10.60% ± 6.9%	1.191 ± 0.051	-0.76% ± 4.3%
1.0	S#1: 250 W & 959 mm/s	1.135 ± 0.059	13.54% ± 5.9%	1.069 ± 0.054	6.89% ± 5.4%
	S#2: 350 W & 1366 mm/s	1.162 ± 0.074	16.24% ± 7.4%	1.109 ± 0.068	10.85% ± 6.8%
	S#3: 370 W & 1772 mm/s	1.100 ± 0.061	10.01% ± 6.1%	1.021 ± 0.064	2.13% ± 6.4%

From the stress analysis results (Table 1), pin designs with a circular cross-section can reduce the stress concentration in a unit cell. The dimensional tolerance study aimed to identify the optimal pin design for which the as-built and the designed geometries have similar dimensions and preserve the circular pin cross-section. The primary challenge for building pins with good dimensional accuracy arises from the heat accumulation during laser melting since the pins are relatively small in size and are built as an overhanging structure. The powder bed is less thermally conductive compared with the solid (Wei et al. (2018)); especially at the bottom surface of a pin where melt tracks are only surrounded by powder, the problem of overheating can often be observed (Wu et al. (2020)). As a result, more overheated molten metal can infiltrate into the powder bed and potentially entrap partially melted particles leading to pin shape irregularity and deviation from the design dimension.

Table 3 summarizes pin dimensional measurements for two arrays with pin diameters of 1.2 and 1.0 mm respectively printed using three different power and speed combinations from the porosity study (Table 2). Figure 5a shows the 2cm x 2cm micro pin array test coupons on the build plate and highlights the cross-section which was later sectioned using electrical discharge machining and characterized by a Keyence VR-5200 white light scanner (see examples in Figure 5b). Every pin in a pin array was measured along the horizontal and vertical directions to derive the mean and deviation values shown in Table 3. The anticipated infiltration effect showed no significant impact on the bottom surfaces resulting in a less severe overprinting situation along the vertical direction compared with the horizontal direction. No clear correlation was observed between the pin dimensions printed using different parameters; however, the S#2 parameter set provided a slightly lower deviation from the design. Overall, the combinations of pin dimensions and process parameters resulted in pin dimensions within ± 8 percent of the design dimensions.

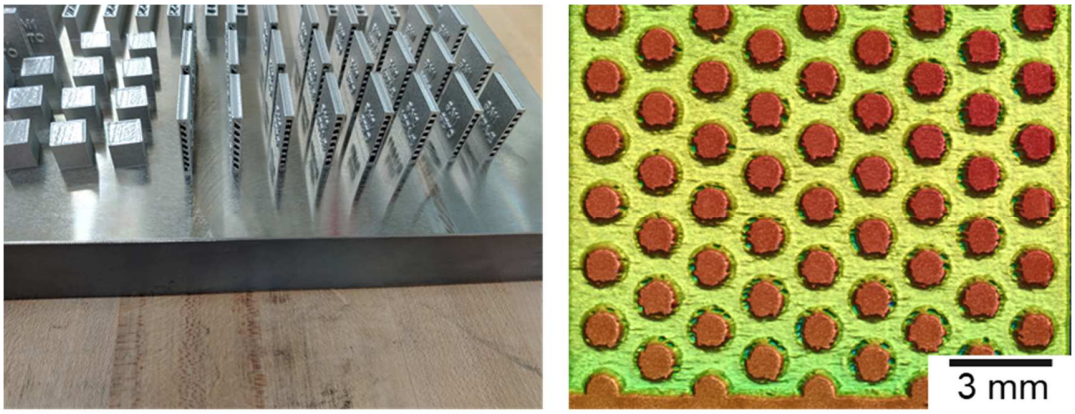

(a) (b)

Figure 5.a) Test cubes and as-built micro pin arrays residing on the build plate. b) The cross-sectional height profiles of the 1.2mm diameter pin array printed using laser parameters of 250 W and 959 mm/s with a hatch spacing of 0.11mm

Surface roughness plays a significant role in affecting the flow pattern and pressure drop in both the MS and sCO_2 sides of the PHE. The plate surface roughness of the pin arrays built using three different laser parameter sets was characterized using the same Keyence VR-5200 white light scanner as used in Figure 5b to assess the impact of the process parameters on as-printed roughness. Figure 6 shows the roughness of the three plates where anisotropic roughness patterns, i.e., AM layer contrast, can be clearly observed. During the operation/testing, the CO_2/MS flows along those layered features. As shown in Table 2, specimen S#3 displayed the highest R_z value as the extruded surface features presented shape of molten droplets while in specimen S#1 the extruded features were much smaller in size, predominantly partially melted powder particles. These droplet-like features are believed to be induced by the over-melting at the end of melt tracks where heat tends to accumulate due to the poor thermal conductivity at the powder-solid interface. Note that the three laser parameter sets corresponded to similar energy densities. That said, as opposed to the energy density which was dictated by both the laser power and speed, the laser power was the more dominant factor for their appearance since the laser comes to a stop at the end of each melt track.

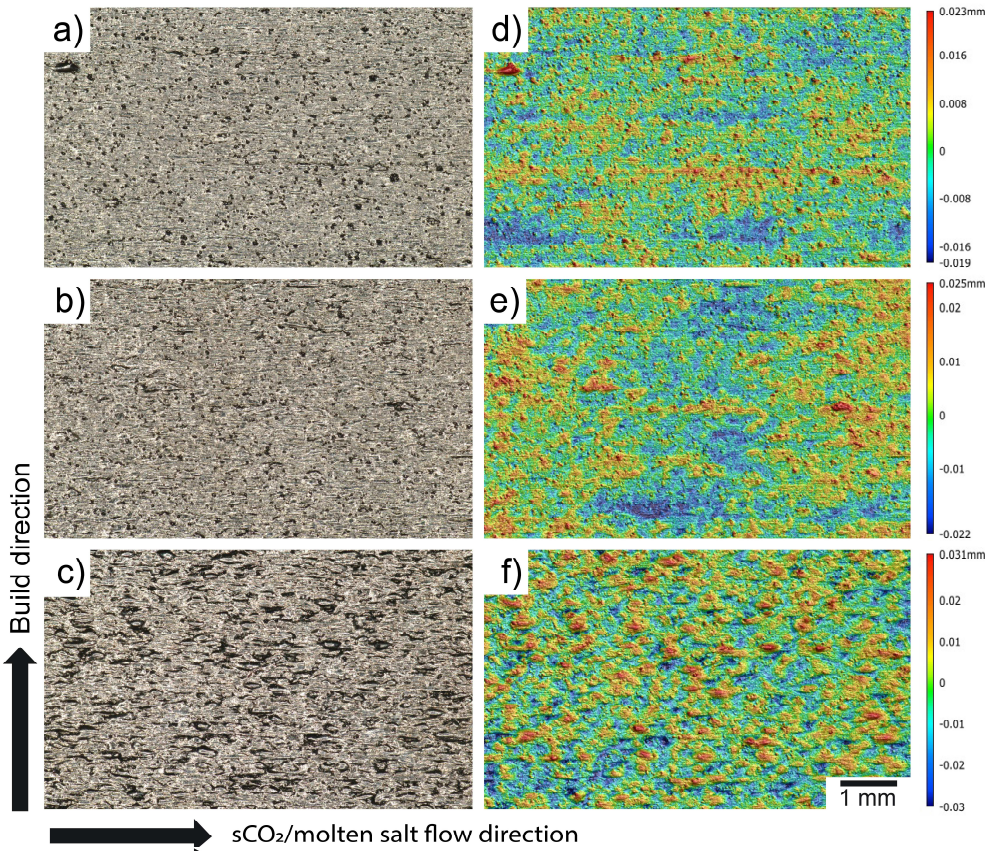

Figure 6. Rough side surfaces of thin wall printed using parameters a) S#1, b) S#2, and c) S#3 as labeled in Table 2 and the corresponding height maps in d) – f).

Simplified thermofluidic model of the PHE Core

The design of the header for mechanical integrity and flow uniformity was described in the previous section, as was the mechanical design of a unit cell of the core. In this section, a simplified model is presented to estimate the thermal performance of the PHE core. Several geometrical parameters of the core shown in Figure 1e and f such as the cold plate spacing, MS-side fin spacing, cold plate pin array design, and flow parameters such as hot and cold flow inlet temperatures, and mass flow rates affect the thermo-fluidic performance of the PHE. Performing detailed CFD simulations over such a wide parameter space is infeasible; hence a simplified thermofluidic numerical model of the PHE core was developed to evaluate the performance of the heat exchanger. The inlet temperature and pressure of molten salt are $T_{H,in}$ = 720 °C and $P_{H,in}$ = 1 bar, respectively. The inlet temperature and pressure of sCO_2 are $T_{C,in}$ = 500 °C and $P_{C,in}$ = 200 bar, respectively.

Figure 7a shows the simplified PHE model, which considers each cross-flow section as a unique control volume and uses the epsilon-NTU approach for heat transfer calculations. The counter-flow region, on the other hand, is divided into differential control volumes to accurately capture property variations in the fluids (Figure 7b). The calculation process, illustrated in a flow chart in Figure 7c, starts at the section labeled "Cross-flow 1" corresponding to the exit of the cold fluid and the inlet of the hot fluid. The known hot fluid inlet temperature T_{hi} is specified, and a reasonable guess for the sCO_2 outlet temperature, T_{co}, is used as input for the cold side.

The thermal behavior of the cross-flow sections is based on the lumped model assumption and a single average temperature is calculated on each side. Upon obtaining the outlet molten salt and inlet sCO_2 for this section which correspond respectively to the inlet hot and outlet cold temperatures for the counter-flow regions ($T_{hi\_counter}$, $T_{co\_counter}$), the model proceeds with the sectional counter-flow region which uses the cross-flow section temperature and pressure outputs as input conditions, and solve differential equations for each subsection of length dx. The cold inlet and hot outlet counter-flow temperatures, $T_{hi\_counter}$ and $T_{co\_counter}$, are finally passed on to the second cross-flow section that outputs cold inlet and hot outlet temperatures T_{ci} and T_{ho}. The calculated cold inlet temperature is compared to the actual known inlet temperature for the sCO_2; if the two differ significantly new guesses made, and a new iteration starts at the first cross-flow section. The process illustrated on the flowchart of Figure 7c is repeated until the two values are within 0.01 ^{o}C. Details of the core model and correlations used for pressure drop and heat transfer coefficient are provided in the appendix.

The high-temperature molten salt used in this study consists of a molar ratio of 20% NaCl, 40 % KCl and 40 % $MgCl_2$. The properties of molten salt depend only on temperature

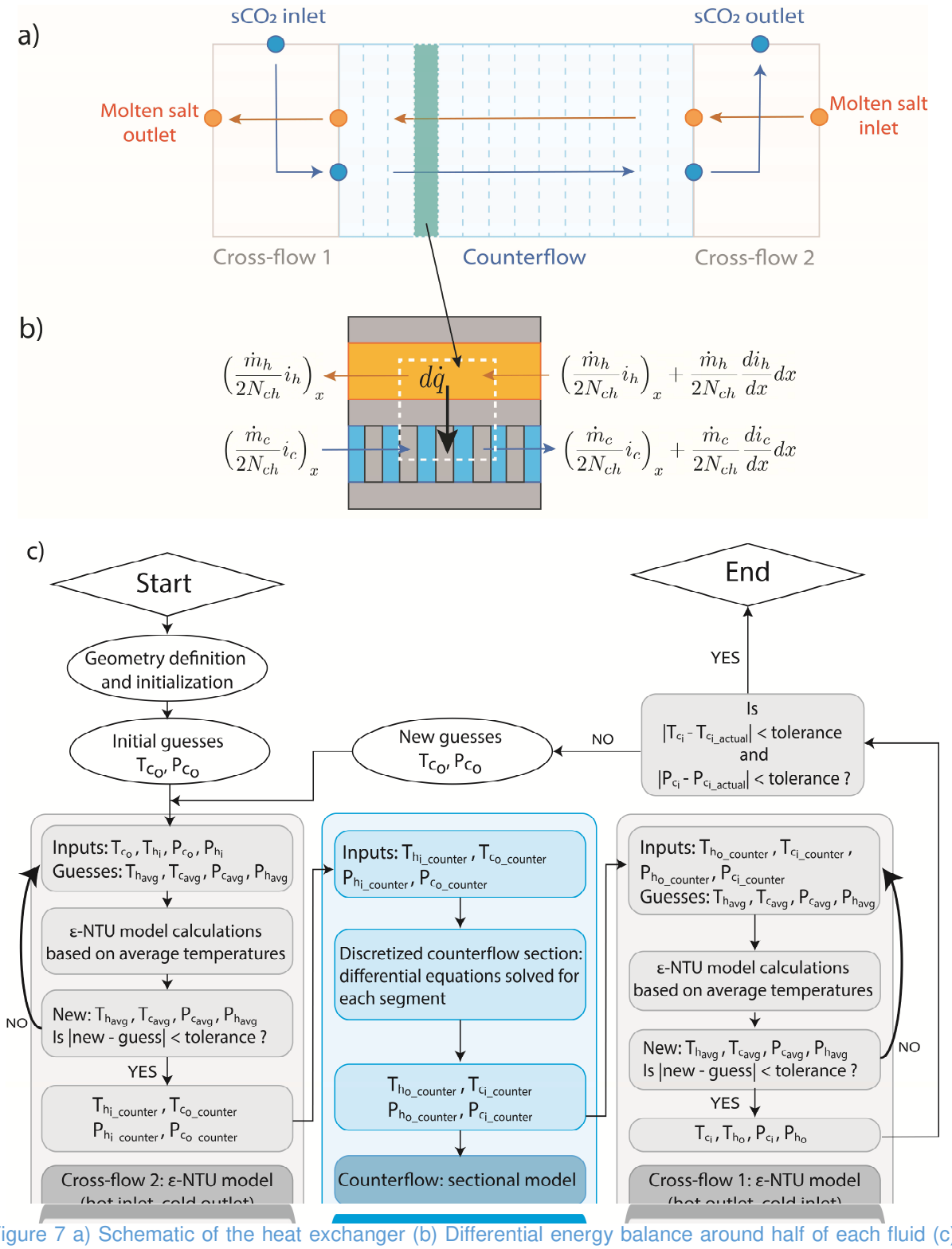

Figure 7 a) Schematic of the heat exchanger (b) Differential energy balance around half of each fluid (c) Simplified numerical model flowchart.

because of incompressibility. The property correlations for density, specific heat capacity, thermal conductivity and viscosity are obtained from Li et al. (2017):

$$\begin{cases} \rho_H(g/cm^3) = -4.06 \times 10^{-4}\, T_H(℃) + 1.8821 \\ c_{p,H}(kJ/kg \cdot K) = -5.2799 \times 10^{-4}\, T_H(℃) + 1.3946 \\ k_H(W/m \cdot K) = -1\, x\, 10^{-4}\, T_H(℃) + 0.5082 \\ \mu_H(Pa \cdot s) = 0.3036 \times exp\left(\frac{2137.3}{T_H(℃) + 273.15}\right) \end{cases} \quad (1)$$

For sCO_2, a property table with the step size of 1K and 0.25 bar was generated in EES (F-Chart Inc). This table covers the temperature range of [753K, 992K] and the pressure range of [192bar, 200bar]. The thermal conductivity of Haynes 282 (Haynes International, 2020) can be expressed as:

$$k_{wall} = 0.019 T_{wall} + 5.963 \quad (2)$$

Process-based Cost Model

The PHE cost (in $/kW-th) is estimated for each set of geometric and flow parameters using a process-based cost model (PBCM). The PBCM estimates the cost to manufacture the PHE based on the costs associated with the individual steps making up the manufacturing process. The constituent costs for each process step include equipment, material, labor, facility, utilities, consumables, and overhead. The PBCM relates constituent costs for each process step, processing parameters, facility operating parameters, and PHE design parameters to determine the total cost. The PBCM models a four-step manufacturing process. In the first step, the part is formed layer-by-layer by melting metal powder via a LPBF method. In the second step, thermal stresses built up in the part are relieved via stress-relief heat treatment. In the third step, the baseplate on which the part is built and support structures are removed via computer numerically controlled bandsaw. In the fourth step, an abrasive medium is forced through the PHE to clean and smooth the internal passages via abrasive flow machining. The cost estimate is provided based on the process parameter set S#2 in Table 2 since this parameter set resulted in relatively fast printing speeds (and hence lower cost), high part density, low surface roughness and good dimensional tolerance. Full details of the cost model are described in Ziev et al. (*available in preprint).*

PARAMETRIC STUDY

Several important parameters play a role in determining the overall size of the PHE; these parameters, along with their baseline values and range of variation are indicated

in Table 4. One parameter was varied at a time to understand the independent influence of each parameter on the PHE design, performance, and cost. The overall dimensions of the core of the PHE were kept fixed at L = 24 cm, based on the dimensions of the build plate in the EOS M290 LPBF machine. The height was fixed at 5 cm based on the ability to distribute the flow uniformly in the counter-flow section of the PHE. The upper limit on the width were also based on the dimensions of the build plate in the machine. The baseline pin diameter (D_{pin}), height (W_c or H_{pin}), and pitch ratio (β_T), were obtained from detailed mechanical stress simulations, see Table 1. The R_z roughness encompasses a range that includes process parameters S#1 and S#2 in Table 2. For ease of comparison across geometric parameters, the scales of the y-axes are kept uniform for all the performance indicators except in cases that have different range or need a better resolution. While the parametric study was performed on all variables in Table 4, only those that showed significant trends are reported here for brevity.

Table 4 . Fixed and varied parameters in PHE design

Parameters	*Baseline Value*	*Range*
L (cm)	24	--
H (cm)	5	--
W (cm) / N_{plates}	10 / 26	[10.00, 18.00] / [26, 47]
W_H (mm)	1.00	[1.00, 2.50]
W_c (mm)	1.80	[0.75, 2.50]
β_T (-)	2.05	[1.34, 2.05]
D_{pin} (mm)	1.20	[0.50, 1.50]
Th_{wall} (mm)	0.50	[0.30, 1.50]
S_{fin} (mm)	5.00	[2.00, 10.00]
Th_h (mm)	1.00	[0.3, 1.00]
R_z (µm)	60	[30.00, 150.00]
$\dot{m}_{sCO2}$ (g/s)	50	50;75
$\dot{m}_{MS}$ (g/s)	74	[64, 148]

Mass Flow Rate Variation

Figure 8 shows the PHE performance as a function of the heat capacity ratio, C_r, defined as the ratio of the minimum heat capacity rate, C_{min}, to the maximum heat capacity rate, C_{max}. The variation of C_r was achieved by changing the MS flow rate within the range specified in Table 4 for a fixed sCO_2 mass flow rate of 50g/s (Figure 8a-b) and 75g/s (Figure 8c-d). Performance indicators of interest include the outlet sCO_2 and MS

temperatures, the PHE effectiveness (Figure 8a, c), and the cost, heat duty and cold-side pressure drop (Figure 8b, d).

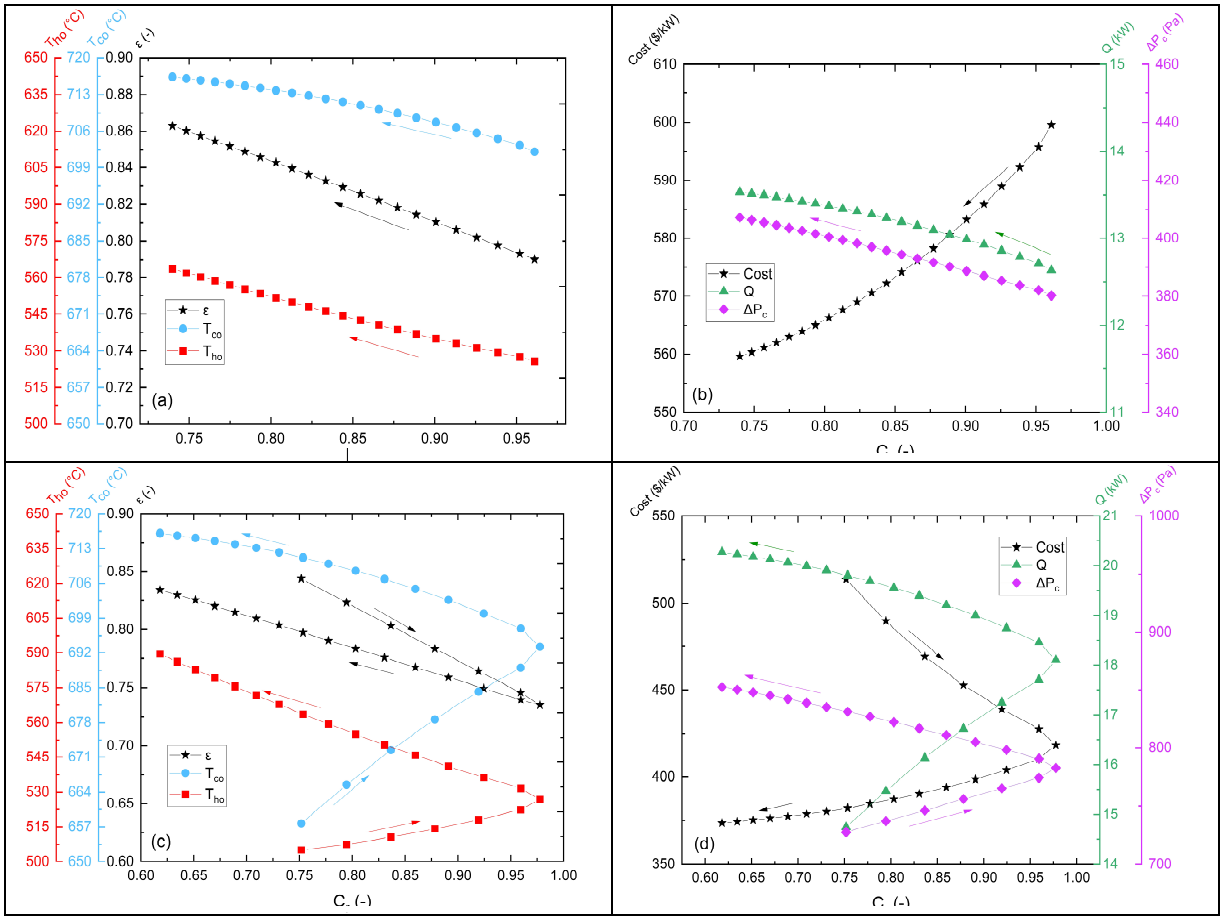

Figure 8. PHE performance predicted by the thermofluidic and cost models for various Cr ratios at sCO_2 flow rate of (a,b) 50g/s and (c,d) 75 g/s (as a reference, the volumetric power density at 13kW corresponds to 6.6 MW/m^3 and at 20kW corresponds to 10.2 MW/m^3). Arrows indicate the direction of increasing MS flow rate.

For the $\dot{m}_{sCO2}$ of 50 g/s, the C_{min} is always on the sCO_2 side, with a low C_r referring to a high MS flow rate and a high C_r corresponding to a low MS flow rate. The performance trends in Figure 8a are monotonic, with the highest effectiveness of 0.86 and outlet sCO_2 temperature 716 ^oC obtained for the largest MS mass flow rate (low C_r). The effectiveness increases with an decrease in C_r from a value of 0.79 at a Cr of 0.96 to a value of 0.86 at a Cr of 0.74, with a corresponding increase in thermal power rating and volumetric power density from 12.6 to 13.5 kW (Figure 8b) and 6.4 to 6.9 MW/m^3, respectively. The overall heat transfer coefficient is relatively unchanged for all C_r since the flow on the MS side is laminar. Since C_{min} is on the sCO_2 side, the NTU is also relatively constant at 10. As a reference, the effectiveness for a pure counter-flow heat

exchanger at a C_r of unity and NTU of 10 is 0.91. An increase in effectiveness is related to an increase in MS flow rate (corresponding to a decrease in C_r), which causes a higher temperature differential along the PHE for heat transfer to sCO_2. The cold side exit temperature increases from 702 °C to 716 °C with a decrease in C_r over the same range, while the MS exit temperature increases by a greater amount from 526 °C to 564 °C. The pressure drop on the cold side (Figure 8b) increases slightly over the range of C_r due to increase in average temperature and a consequent increase in viscosity of sCO_2.

Performance trends for the higher sCO_2 flow rate of 75 g/s, shown in Figure 8c-d, display a non-monotonic trend. For this condition as well, the UA is relatively constant due to laminar flow conditions in the MS side and the fixed flow rate on the sCO_2 side. However, with an increase in MS mass flow rate, C_{min} is on the hot side and varies with MS flow rate between 64 g/s to 84 g/s, (corresponding to C_r from 0.75 to 0.96), before switching to the cold side. This increase in C_{min} at a fixed UA causes a decrease in NTU and a corresponding decrease in effectiveness from 0.84 to 0.74. Further increase in MS flow rate beyond 84 g/s results in a fixed C_{min} value based on the cold side flow rate and causes a decrease in C_r from unity to 0.62 with increase in MS flow rate from 84 g/s to 148 g/s. In this range, the trend is similar to that seen in Figure 8a with the thermal rating and effectiveness increasing with a decrease in C_r. The exit temperatures of MS and sCO_2 increase with an increase in MS flow rate; the increase in average fluid temperature on the cold side results in a higher pressure drop (Figure 8d).

The selection of the optimal operational point is a function of several parameters with contrasting variations. The minimum sCO_2 outlet temperature for the power cycle based on DOE requirements is 700 °C (Mehos et al. (2017)). However, in order to reduce parasitic losses associated with the MS loop, it is also important to exit the PHE with the lowest feasible MS temperature. It is possible to define an operational window that spans the two sCO_2 flow rates considered. A 50g/s sCO_2 flow rate associated with a C_r of 0.81 and 74 g/s of molten salt would yield a 13.3 kW power output, an outlet temperature of 713 °C for the sCO_2 and 550 °C for the molten salt, with a sCO_2 pressure drop of 400 Pa. The same T_{ho} temperature can be achieved with a C_r of 0.83 and 75g/s of sCO_2 and 108 g/s of molten salt. The power output in this case is higher (19.4 kW) and the sCO_2 pressure drop would increase to 817 Pa. The latter configuration can be a preferred option for increased thermal power rating of the PHE; however, its effectiveness, at 0.78, is lower than the 0.84 effectiveness at the lower sCO_2 flow rate condition. Higher thermal rating and effectiveness can be obtained by increasing the MS flow rate at both sCO_2 flow rates; however, at the penalty of higher MS exit temperature. In the scenarios considered so far, the volume of the heat exchanger is

kept constant so changes in PHE cost (in $/kW-th) are dictated by the thermal power rating. For the 50g/s of sCO_2 flow rate, an increase in power rating from 12.6 to 13.5 kW allows a cost reduction from $600/kW-th to approximately $560/kW-th. In the 75 g/s case, the larger variation in power output from 14.7 to 20.2 kW results in a cost reduction of $145/kW-th, from $520/kW-th to $375/kW-th.

Heat exchanger overall width (W_{max}) / N_{plates}

Figure 9a-b shows the influence of the overall width (W_{max}) on the performance parameters of the PHE. Variation in the width, with all other parameters in Table 4 being held constant, results in an increase in the number of hot and cold plates available for heat transfer as noted in Figure 9a. For a fixed flow rate of 50 g/s for sCO_2 and 74 g/s for MS, the exit temperature of the hot stream decreases while that of the cold stream increases with number of plates due to the increase in residence time for heat exchange. Consequently, the heat exchanger effectiveness increases from 0.83 to 0.88. The thermal rating of the PHE increases modestly from 13.3 kW to 13.6 kW (Figure 9b); however, the increase in width increases the volume of the PHE more significantly and hence the volumetric energy density decreases from 6.8 to 4.6 MW/m^3. Over the range of variation of number of plates per unit width, the cold side pressure losses are more than halved, decreasing from 350 to 125 Pa due to the reduced mass flow rate through each plate. In this scenario, the cost is higher by almost $65/kW-th because the increase in W_{max} from 10 to 18 cm translates into an increase in material cost in the absence of significant increase in heat transfer rate.

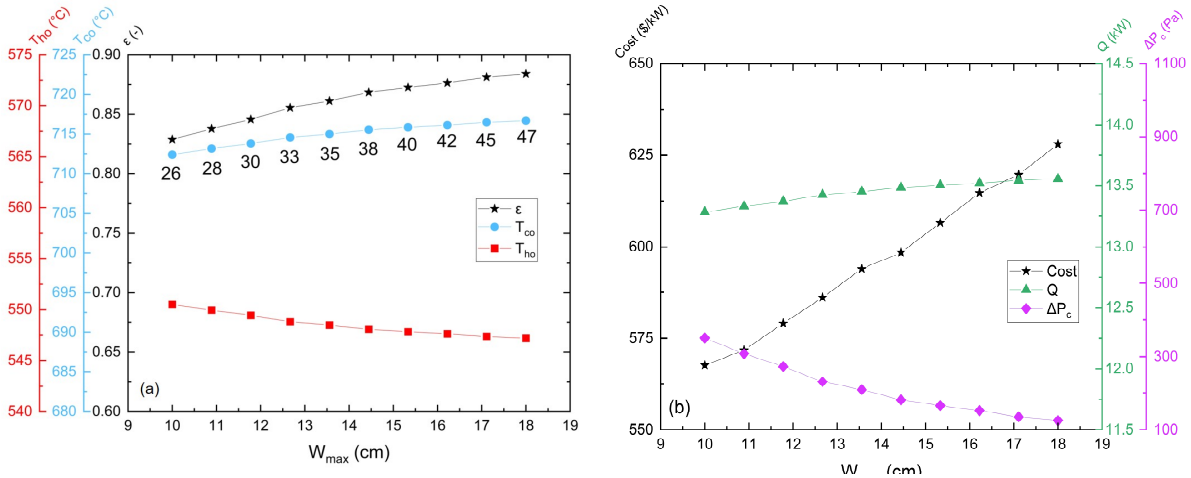

Figure 9. Parametric study of variation in PHE width, W_{max} varying from 10 to 18cm: (a) T_{ho}, T_{co}, and ε variation and (b) $/kW-th, ΔP_c, and thermal rating variation with W_{max}. sCO_2 and MS flow rate of 50 and 74 g/s respectively.

Hot channel width (W_h)

Figure 10 shows how the hot channel width (W_h) impacts the performance of the PHE. As the hot channel width increases from 1 to 2.5 mm, the performance of the heat exchanger is adversely impacted, and the overall efficiency decreases from 0.83 to 0.63.

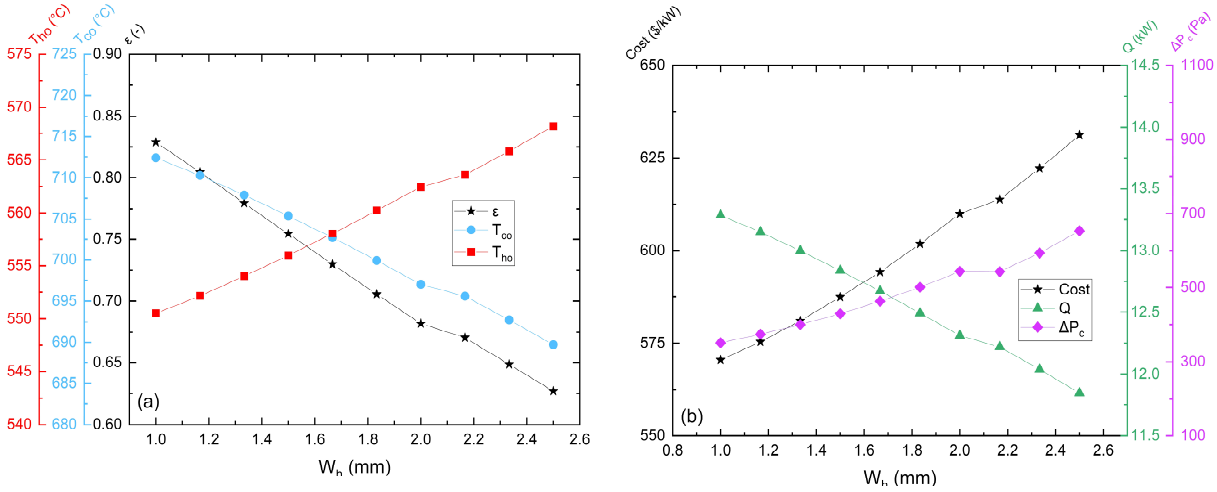

Figure 10. Parametric study of variation in MS channel width, W_h, varying from 1 to 2.5 mm: (a) T_{ho}, T_{co}, and ε variation and (b) $/kW-th, ΔP_c, and thermal rating variation with W_h. sCO2 and MS flow rate of 50 and 74 g/s respectively.

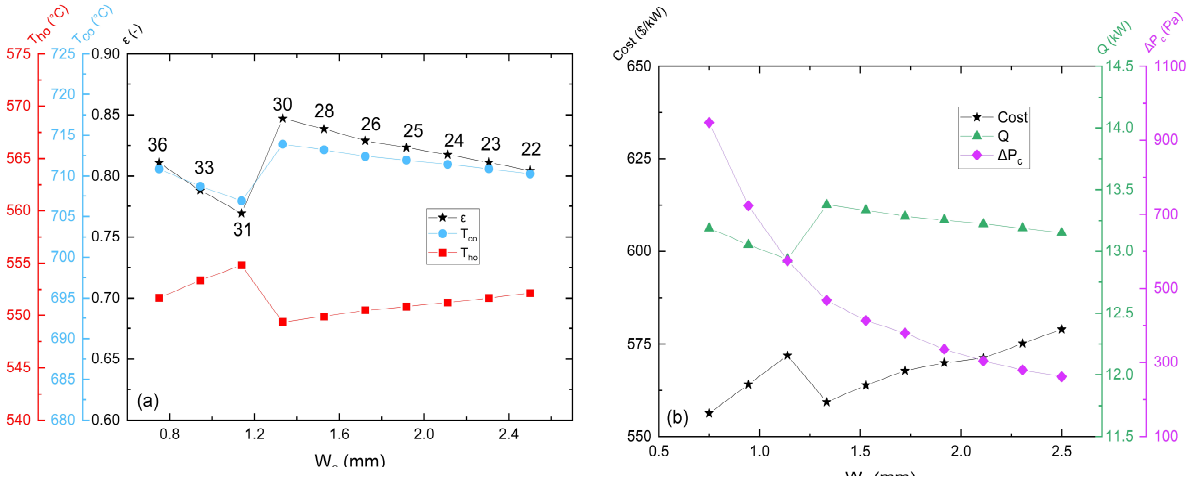

Figure 11. Parametric study of variation in sCO_2 channel width, W_c, varying from 0.75 mm to 2.5 mm: (a) T_{ho}, T_{co}, and ε variation and (b) $/kW-th, ΔP_c, and thermal rating variation with W_h. sCO_2 and MS flow rate of 50 and 74 g/s respectively.

This behavior is observed because fewer plates are available for heat transfer and in each plate, the residence time of the hot stream is no longer sufficient to transfer the same amount of heat to the cold side. As a result, the power output decreases from 13.3 to 11.8 kW. The total solid volume also decreases but only marginally so that the volumetric power density decreases from 6.8 to 6.0 MW/m^3. The pressure drop on the sCO_2 side increases from 351 to 653 Pa because the flow rate in each plate increases with

fewer hot and cold plate pairs available. The cases with W_h of 2.0 and 2.2 mm display an almost identical pressure drop and less steep gradients for the other performance parameters because the number of plates is the same. Unlike the other cases where the increase in value of W_h is sufficient to cause the number of plates to decrease by 1, the case with W_h of 2.2 mm is a rare occurrence of N_{plate} remaining constant and induces the plateau observed between W_h values of 2.0 and 2.2mm. Similar to the volumetric power density, the increase in W_h causes a minor decrease in total volume and therefore a small reduction in material expenditure but the significant reduction in power output induces an overall increase in cost from $570 /kW-th to $ 630 /kW-th.

Cold channel width (W_c)

The effect of varying the sCO_2 channel width from 0.75 to 2.5 mm is illustrated in Figure 11. As the channel width increases, the residence time of the sCO_2 decreases due to lower number of plates, resulting in lower cold and higher hot outlet temperatures. These trends are observed in Figure 11 except from the case with plate number of 31 to 30, where the aspect ratio of the pin begin to assume values greater than unity, and the flow transition to a regime in which vortex shedding is expected based on the chosen correlation for heat transfer in pin arrays (Rasouli et al. (2017)) (see Appendix). Because of the performance jump observed from a W_c of 1.1 mm to 1.3 mm, the upper and lower limit of the performance markers such as efficiency, temperature and power output are not observed at the boundaries of the W_c range considered but rather at that discontinuity. At the transition, the efficiency jumps from 0.77 to 0.85 and the volumetric power density increases from 6.6 to 6.8 MW/m^3. The pressure drop is the only parameter that displays a monotonic trend and shows values which is significantly different at W_c of 0.75 and 2.5mm, decreasing from a value of 947 to 261 Pa. The cost varies between $555 /kW-th and $580 /kW-th with a drop when the aspect ratio exceeds unity and vortex shedding enhances the thermal performance. Changing the width of the cold channel does not impact the volume significantly and the cost trend observed in this case is determined by changes in the power output.

Discussion on parametric trends

From the results of single-effect parametric variations, one can arrive at a desired design for the AM PHE. The width (number of hot-cold core pairs) of the PHE can be scaled to increase the thermal rating. The height is kept fixed at 5 cm based on a balance between minimizing cross-flow sections at the inlet and exit and uniform flow distribution within the plate. Both the overall length and width of the PHE are constrained by the dimensions of the LPBF build plate. Given these constraints, keeping W_c at 1 mm and

W_h at 1.35 mm provides the best geometrical design. This design corresponds to the peak value of effectiveness shown in Figure 11.

For this design and for a flow rate of 50 g/s on the sCO_2 side and 74 g/s on the MS side, an effectiveness of 0.85, a thermal rating of 13.4 kW, a power density of 6.85 MW/m^3 (11.2 MW/m^3 for core alone), can be achieved at a cost of $560 /kW-th. The heat transfer coefficient on the hot (MS) side is 2.7 times lower than that on the sCO_2 side, indicating that improvements on the MS side for heat transfer coefficient or/and surface area will result in a higher power density and lower cost. Future work on how to improve the PHE performance by a reduction of the hot side resistance is needed to further reduce cost and increase the power density.

It should be noted that, while it is critical for powder removal from internal passages to be fully effective in post-processing, surface roughness has a minor effect on the thermo-fluidic performance of the PHE. With an increase in surface roughness from 30 to 150 μm, the sCO_2 pressure drop increases from 374 to 494 Pa and the power output marginally increases from 13.3 to 13.4 kW. Hence, from a thermo-fluidic performance standpoint, the focus of post-processing should be primarily on powder removal as opposed to reduction in surface roughness. The PHE design did not consider MS corrosion and its effect on the heat exchanger structural integrity. Studies of corrosion rates are required to assess how the heat exchanger performance would be impacted and whether the magnitude of corrosion is such that both the structural and thermofluidic aspects of the design need revision, such as increasing the thickness walls between the fluids. Based on the model, increasing the wall thickness from the baseline value of 0.5 mm to 1 mm will result in a 4.8 % decrease in effectiveness and a 1.4 % decrease in thermal rating of the PHE.

Table 5. Comparison of thermo-fluidic performance of PHEs with different core lengths

AM machine	PHE length (m)	$\dot{m}_{sCO2}$ (kg/s)	$\dot{m}_{MS}$ (kg/s)	C_r	q (kW)	Power density, including headers (MW/m^3)	ε	ΔP_{sCO2} (kPa)	ΔP_{MS} (kPa)	T_{ho} (°C)
EOS M290	0.24	0.050	0.075	0.80	13.4	6.86	0.85	0.54	0.56	551
GE Additive 2000R	0.80	0.19	0.288	0.80	51.2	10.8	0.90	25.3	7.1	552

The AM PHE design presented here provides high power densities while maintaining very low pressure drops on both sCO_2 and MS sides (< 1 kPa for sCO_2 and MS). The upper limit on the PHE length was restricted to 24 cm based on the dimensions of the EOS M290 LPBF machine which was used for printing and cost analysis reported in this

paper. However, industrial AM machines such as the GE Additive (Concept Laser) metal X line 2000R, allow for build lengths of 80 cm and width of up to 40 cm. If the selected PHE design from the parametric study were to be 80 cm in length instead of 24 cm, with all other parameters kept the same, a significant increase thermal performance can be achieved, as shown in Table 5, at the expense of higher pressure drop. This pressure drop is still only 0.125 % of the line pressure of 200 bar. It should be noted that the pressure drop with the longer PHE is low when compared to designs in literature; for instance, the design sCO_2 pressure drop in Caccia et al. (2018) was 100 kPa. If the number of hot/cold plates were scaled up to the 40 cm width of the X line 2000R, the resulting PHE would have a thermal rating of 205 kW. Further scaling up to MW-scale PHE can be obtained by numbering up such 205 kW modules by welding header tubes.

CONCLUSIONS

Design of an additively manufactured (AM) nickel superalloy molten salt (MS)-to-supercritical carbon di-oxide (sCO_2) primary heat exchanger (PHE) was described. The PHE design was based on pressurized pin array plates through which sCO_2 flows, separated by straight channels through which MS flows. Details of structural design and flow distribution in the pin array and headers were discussed. Correlation-based thermofluidic, and a process-based cost models were developed to evaluate the performance and assess the cost implications of MS-sCO_2 AM PHEs for concentrated solar power applications. The following salient conclusions can be drawn from the presented work:

1. Co-design considering mechanical, thermofluidic, AM fabrication, and cost is necessary for viable and compact high-temperature and high-pressure PHE designs for AM;
2. High part density and dimensional accuracy have been demonstrated using laser powder bed fusion AM printing and alloy H282;
3. AM designs can yield high power density, high effectiveness designs in the range of 6-10 MW/m^3 for the PHE within the constraints of 550 ^oC exit fluid temperature on the hot side;
4. A tradeoff exists between high power density (and hence cost) and exit temperature of the MS for fixed inlet temperature of the fluids. Lower exit MS temperature would result in a lower power density and higher cost. Similarly, a tradeoff exists between a desired exit temperature of the hot (MS) and cold fluids (sCO_2) and minimum heat capacity rate ratio. Specific to the inlet temperatures in this application, the minimum heat capacity rate is on the sCO_2 side in order for exit temperatures in excess of 700 ^oC to be achieved;

5. A parametric study using the thermofluidic model indicates that a smaller width on the MS side, W_h, and a pin height in the range that permits vortex shedding, enables the highest effectiveness and power density;
6. An increase in the length of the core from 24 cm to 80 cm results in a 6 % increase in effectiveness, from 0.85 to 0.90, and a 58 % increase in power density, from 6.86 MW/m^3 to 10.8 MW/m^3. The pressure drop for the 80 cm-long PHE is only 0.125 % of the line pressure on the cold side.

The AM fabrication costs are based on a single-laser EOS machine, typically used in a research environment. Further reductions in cost can be achieved through use of multi-laser machines, process refinements (e.g., laser beam shaping or dithering) that allow for higher printing speeds, and industrial engineering improvements that either reduce material handling or allow it to take place outside the AM machine.

REFERENCES

1. Caccia, M., Tabandeh-Khorshid, M., Itskos, G., Strayer, A.R., Caldwell, A.S., Pidaparti, S., Singnisai, S., Rohskopf, A.D., Schroeder, A.M., Jarrahbashi, D., Kang, T., Sahoo, S., Kadasala, N.R., Marquez-Rossy, A., Anderson, M.H., Lara-Curzio, E., Ranjan, D., Henry, A., Sandhage, K.H., 2018. Ceramic–metal composites for heat exchangers in concentrated solar power plants. Nature, Vol 562, pp. 406-409.
2. Chu, W.X., Bennett, K., Cheng, J., Chen, Y.T., Wang, Q.W., 2019. Thermo-hydraulic performance of printed circuit heat exchanger with different cambered airfoil fins. Heat Transfer Engineering, Vol 41(8), pp 708-722.
3. Cormier, Y., Dupuis, P., Farjam, A, Corbeil, A., Jodoin, B., 2014. Additive manufacturing of pyramidal pin fins: Height and fin density effects under forced convection. International Journal of Heat and Mass Transfer, Vol 75, pp. 235-244.
4. Dupuis, P., Cormier, Y., Fenech, M., Corbeil, A., Jodoin, B., 2016. Flow structure identification and analysis in fin arrays produced by cold spray additive manufacturing. International Journal of Heat and Mass Transfer, Vol 93, pp. 301-313.
5. Ferster, K. K., Kirsch, K. L., and Thole, K. A., 2017. Effects of geometry, spacing, and number of pin fins in additively manufactured microchannel pin fin arrays. Journal of Turbomachinery, Vol 140(1), p. 011007.
6. Greiciunas, E., Borman, D., Summers, J., Smith, S.J., 2019. A numerical evaluation of next generation additive layer manufactured inter-layer channel heat exchanger. Applied Thermal Engineering, Vol 162, Article 114304.
7. HAYNES 282 alloy (online brochure), 2020. Haynes International. Last accessed online in July 23, 2021 at http://haynesintl.com/docs/default-source/pdfs/new-alloy-brochures/high-temperature-alloys/brochures/282-brochure.pdf?sfvrsn=20
8. Ho, J.Y., Wong, K.K., Leong, K.C., Wong, T.N., 2017. Convective heat transfer performance of airfoil heat sinks fabricated by selective laser melting. International Journal of Thermal Sciences, Vol 114, pp. 213-228.
9. Ho, J.Y., Leong, K.C., Wong, T.N., 2020. Additively-manufactured metallic porous lattice heat exchangers for air-side heat transfer enhancement. International Journal of Thermal Sciences, Vol 150, Article 119262.
10. Ibrahim, O.T., Monroe, J.G., Thompson, S.M., Shamsaei, N., Bilheux, H., Elwany, A., Bian, L., 2017. An investigation of a multi-layered oscillating heat pipe additively manufactured from Ti-6Al-4V powder. International Journal of Heat and Mass Transfer, Vol 108, pp. 1036-1047.

11. Jing, Q., Xie, Y., Zhang, D., 2020. Thermal hydraulic performance of printed circuit heat exchanger with various channel configurations and arc ribs for SCO_2 Brayton cycle. International Journal of Heat and Mass Transfer, Vol 150, Article 119272.

12. Kandlikar, S. G., Schmitt, D., Carrano, A. L., and Taylor, J. B., 2005. Characterization of surface roughness effects on pressure drop in single-phase flow in minichannels. Physics of Fluids, 17(10), 100606.

13. Kapoor, M., Dogan, O., Rozman, K., Hawk, J., Wilson, A., L'Estrange, T., Narayanan, V., 2016. Diffusion bonding of H230 Ni-superalloy for application in microchannel heat exchangers. 5th International sCO_2 Power Cycles Symposium, San Antonio, TX, March 28-31.

14. Katz, A., Aakre, S.R., Anderson, M.H., Ranjan, D., 2021. Experimental investigation of pressure drop and heat transfer in high temperature supercritical CO_2 and helium in a printed-circuit heat exchanger. International Journal of Heat and Mass Transfer, Vol 171, Article 121089.

15. Khalesi, J., Sarunac, N., 2019. Numerical analysis of flow and conjugate heat transfer for supercritical CO_2 and liquid sodium in square microchannels. International Journal of Heat and Mass Transfer, Vol 132, pp. 1187-1199.

16. Kirsch, K.L., Thole, K.A., 2016. Heat transfer and pressure loss measurements in additively manufactured wavy microchannels. Journal of Turbomachinery, Vol 139 (1), 011007.

17. Kirsch, K.L., Thole, K.A., 2017. Pressure loss and heat transfer performance for additively and conventionally manufactured pin fin arrays. International Journal of Heat and Mass Transfer, Vol 108, pp. 2502–2513.

18. Larson, F.R., Miller, J., 1952. Time-temperature relationship for rupture and creep stresses. Transactions of ASME, 74, 765-771.

19. Li, Y., Xu X., Wang X., Li P., Hao Q., Xiao, B., 2017. Survey and evaluation of equations for thermophysical properties of binary/ternary eutectic salts from NaCl, KCl, MgCl2, CaCl2, ZnCl2 for heat transfer and thermal storage fluids in CSP. *Solar Energy* 152:57-79.

20. Li, W., Yu, G., Yu, Z., 2020. Bioinspired heat exchangers based on triply periodic minimal surfaces for supercritical CO_2 cycles. Applied Thermal Engineering, Vol 179, Article 115686.

21. Mehos, M., Turchi, C., Vidal, J., Wagner, M., Ma, Z., Ho, C., Kolb, W., Andraka, C.,

Kruizenga, A., 2017. Concentrating solar power gen 3 demonstration roadmap. technical report NREL/TP-5500-67464.

22. Miller, R. W. 1996, Flow measurement engineering handbook. McGraw-Hill, New York, 3rd edition.

23. Moody, L. F., 1944. Friction factors for pipe flow. Trans. ASME, 66:671–684.

24. Moores, K. A., and Joshi, Y. K., 2003. Effect of tip clearance on the thermal and hydrodynamic performance of a shrouded pin fin array. J. Heat Transfer, vol. 125, no. 6, pp. 999-1006.

25. Nellis, G., Klein, S., 2009. Heat Transfer. Cambridge.

26. Ngo, T.D., Kashani, A., Imbalzano, G., Nguyen, K.T.Q., Hui, D., 2018. Additive manufacturing (3D printing): a review of materials, methods, applications and challenges. Compos. B Eng., Vol 143, pp. 172-196.

27. Pandey, V., Kumar, P., Dutta, P., 2020. Thermo-hydraulic analysis of compact heat exchanger for a simple recuperated sCO₂ Brayton cycle. Renewable and Sustainable Energy Reviews, Vol 134, Article 110091.

28. Peles, Y., A. Koşar, C. Mishra, C.J. Kuo, and B. Schneider. 2005. Forced convective heat transfer across a pin fin micro heat sink. I. J. Heat Mass Transfer. 48(17): 3615-27.

29. Prasher, R. S., Dirner, J., Chang, J. Y., Myers, A., Chau, D., He, D., Prstic, S., 2007. Nusselt number and friction factor of staggered arrays of low aspect micropin–fins under cross flow for water as fluid. J. Heat Transfer, vol. 129(2), pp. 141-153.

30. Rasouli, E., Naderi, C., Narayanan, V., 2017. Pitch and aspect ratios effects on single-phase heat transfer through microscale pin fin heat sinks. International Journal of Heat and Mass Transfer, Vol. 118, pp. 416-428, https://doi.org/10.1016/j.ijheatmasstransfer.2017.10.105

31. Saeed, M., Kim, M.-H., 2019. Thermal-hydraulic analysis of sinusoidal fin-based printed circuit heat exchangers for supercritical CO₂ Brayton cycle. Energy Conversion and Management, Vol 193, pp. 124-139.

32. Shi, H.Y., Li, M.J., Wang, W.Q., Qiu, Y., Tao, W.Q., 2020. Heat transfer and friction of molten salt and supercritical CO₂ flowing in an airfoil channel of a printed circuit heat exchanger. International Journal of Heat and Mass Transfer, Vol 150, Article 119006.

33. Short, B. E., Raad, P. E., and Price, D. C., 2002a. Performance of pin fin cast aluminum cold walls, part. 1: friction factor correlations. J. Thermophysics and Heat Transfer, vol. 16(3), pp. 389-396.

34. Short, B. E., Raad, P. E., Price, D. C., 2002b. Performance of pin fin cast aluminum cold walls. Part 2: Colburn j-factor correlations. J. Thermophysics and Heat Transfer, vol. 16, pp. 397–403.

35. Snyder, J.C., Stimpson, C.K., Thole, K.A., Mongillo, D.J., 2015. Build direction effects on microchannel tolerance and surface roughness. Journal of Mechanical Design, Vol. 137 (11), 111411.

36. Stimpson, C.K., Snyder, J.C., Thole, K.A., Mongillo, D., 2016. Roughness effects on flow and heat transfer for additively manufactured channels. Journal of Turbomachinery, Vol 138 (5), 051008.

37. Stimpson, C.K., Snyder, J.C., Thole, K.A., Mongillo, D., 2017. Scaling roughness effects on pressure loss and heat transfer of additively manufactured channels, Journal of Turbomachinery, Vol 139 (2), 021003.

38. Tsopanos, S., Sutcliffe, C., Owen, I., 2005. The manufacture of micro cross-flow heat exchangers by selective laser melting. Proceedings of Fifth International Conference on Enhanced, Compact and Ultra-Compact Heat Exchangers: Science, Engineering, and Technology, Hoboken, NJ, CHE2005-53, pp. 410–417.

39. Wang, W.Q., Qiu, Y., He, Y.L., Shi, H.Y., 2019. Experimental study on the heat transfer performance of a molten-salt printed circuit heat exchanger with airfoil fins for concentrating solar power. International Journal of Heat and Mass Transfer, Vol 135, pp. 837-846.

40. Wei, L.C., Ehrlich, L.E., Powell-Palm, M.J., Montgomery, C., Beuth, J., Malen, J.A., 2018. Thermal conductivity of metal powders for powder bed additive manufacturing. Addit Manuf 21:201–208. https:// doi.org/10.1016/j.addma.2018.02.002

41. Wu, Z., Sneha, P.N., Rollett, A.D., 2020. Exploring the fabrication limits of thin-wall structures in a laser powder bed fusion process. The International Journal of Advanced Manufacturing Technology 110.1: 191-207.

42. Zhang, H., Guo, J., Huai, X., Cheng, K., Cui, X., 2019. Studies on the thermal-hydraulic performance of zigzag channel with supercritical pressure CO_2. Journal of Supercritical Fluids, Vol 148 , pp. 104-115.

43. Ziev, T. L., Rasouli, E., Tano, I-N., Wu, Z., Yarasi, S. R., Lamprinakos, N., Narayanan, V., Rollett, A.D., Vaishnav, P., 2021. Economics of an additive manufactured heat exchanger for concentrating solar power. In review.

44. Zukauskas, A. 1972. Heat transfer from tubes in cross-flow. Advances in Heat Transfer, vol. 8, Academic, New York, pp. 93-160.

45. Zukauskas, A., and Ulinskas, R., 1983. Single-phase fluid flow: banks of plain and finned tubes. Heat Exchanger Design Handbook, Washington Hemisphere Publishing, New York, Chap. 2.2.4.

ACKNOWLEDGEMENTS

This material is based upon work supported by the U.S. Department of Energy's Office of Energy Efficiency and Renewable Energy (EERE) under the Solar Energy Technologies Office Award Number DE-EE0008536. Simulations of the unit cell core were performed using computational resources sponsored by the Department of Energy's Office of Energy Efficiency and Renewable Energy and located at the National Renewable Energy Laboratory. The authors acknowledge the help of Dr. Antash Najib in the initial development of the cross-flow model.

DISCLAIMER

The views expressed herein do not necessarily represent the views of the U.S. Department of Energy or the United States Government.

APPENDIX- THERMO-FLUIDIC MODEL

An overview of the model was presented in Figure 7. This appendix provides the equations used in the model, including the counter-flow section, the cross-flow section, and the correlations used for pressure drop and heat transfer coefficient. Comparison of the pin array correlations with CFD simulations of a symmetric strip of the core is used to select the correlations for the model.

A1. Counter-flow Section Model

A sectional model is used for the counter-flow region to capture property variations along the length of the PHE. A schematic of the differential control volumes used for energy balance in the counter-flow region is shown in Figure 7b. The energy balance on the hot side can be written as

$$d\dot{q} + \frac{\dot{m}_H}{2N_p}\frac{di_H}{dx}dx = 0 \tag{A1}$$

where i_H represents the local enthalpy of the hot side and N_p is the number of pairs of hot and cold channels.

Assuming that the axial pressure gradient is small relative to the temperature gradient, the enthalpy gradient can be represented as a temperature gradient,

$$d\dot{q} + \frac{\dot{m}_H}{2N_p}c_H\frac{dT_H}{dx}dx = 0 \tag{A2}$$

The heat transfer rate from the hot to the cold stream is governed by the ratio of the local bulk temperature difference between both streams and the total thermal resistance in the path of heat flow,

$$d\dot{q} = \frac{(T_H - T_C)}{\left\{\frac{1}{\eta_{oH}dA_{tH}h_H} + \frac{th_w}{k_w dA} + \frac{1}{\eta_{oC}dA_{tC}h_C}\right\}} \tag{A3}$$

where h_o is the overall surface efficiency, dA_t is the total area on the hot or cold side for heat transfer, dA is the differential planar based area between the two streams, th_w is the thickness of the wall separating the fluids, and h is the convective heat transfer coefficient. Combining (A2-3), the temperature gradient on the hot side can be expressed as

$$\frac{dT_H}{dx} = \frac{-2N_p}{\dot{m}_H c_H}\frac{(T_H - T_C)}{\left\{\frac{1}{\eta_{oH}dA_{tH}h_H} + \frac{th_w}{k_w dA} + \frac{1}{\eta_{oC}dA_{tC}h_C}\right\}} \tag{A4}$$

A similar expression can be developed for the cold side temperature gradient. The heat transfer coefficient on the cold side is obtained from correlations in literature on flow

through microscale pin arrays (described in Section A3 of the appendix) while that on the hot side is obtained using duct flow relations. The pressure gradient on hot and cold side is obtained using

$$\left.\frac{dp}{dx}\right|_H = -\frac{f_H}{D_h}\frac{\rho_H v^2}{2} \tag{A5}$$

$$\left.\frac{dp}{dx}\right|_C = -f_c\frac{\rho_c v^2}{2}\frac{N_L}{L} \tag{A6}$$

where the friction factor for the hot side, f_H, is obtained from fully developed duct flow relations and for the cold side, f_c, is obtained from correlations in literature for cross flow through tube banks and pin arrays (described in Section A3 of the appendix).

A2. Cross-flow Section model

The cross-flow section starts with an initial guess for the outlet salt and inlet sCO_2 temperatures and pressures for this section. From these guesses, an average between the inlet and the outlet of the cross-flow section is calculated on each side. Fluid and solid properties are evaluated at these average temperatures. The cold inlet temperature, T_{ci}, is evaluated by equating the cold side energy balance with the heat rate obtained from the ε-NTU relationship,

$$\dot{q}_{cr} = C_c(T_{co} - T_{ci}) = Fcorr * \varepsilon C_{min}(T_{hi} - T_{ci}) \tag{A7}$$

where $\dot{q}_{cr}$ is the heat transfer rate in the cross-flow region, and ε is the cross-flow effectiveness, and F_{corr} is a calibration factor to account for the actual flow configuration. The modeled geometry in the core model (Figure 7a) is a simplified version of the actual PHE geometry. Since the actual flow path from the inlet tubes feeding the flow from the header is not truly in cross-flow to the MS path, the effectiveness of this inlet section is expected to lie in between that of a counter-flow and cross flow. The calibration factor, F_{corr} is determined based on comparison with CFD simulations of a half-height plate (Figure 3); see Section A4 of the appendix.

The effectiveness is calculated using the analytical expression for cross-flow heat exchangers with one side mixed (sCO_2) and other side unmixed (MS) (Nellis and Klein (2009),

$$\varepsilon = \left(\frac{1}{C_r}\right)(1 - exp\{-C_r[1 - exp(-NTU_{cr})]\} \text{ for } C_{max} \text{ mixed and } C_{min} \text{ unmixed} \tag{A8}$$

$$\varepsilon = 1 - exp\left(\frac{1 - exp[-C_r(NTU_{cr})]}{-C_r}\right) \text{ for } C_{min} \text{ mixed and } C_{max} \text{ unmixed} \tag{A9}$$

where C_{min} is the minimum of the hot and cold heat capacity rates and C_{max} is the maximum heat capacity rate side and the heat capacity rate ratio is calculated as

$$C_r = \frac{C_{min}}{max(C_c, C_h)} \tag{A10}$$

The number of transfer units for the cross-flow section, NTU_{cr}, in Eqs. A8-A9 is obtained as

$$NTU_{cr} = \frac{UA_{cr}}{C_{min}} \tag{A11}$$

where the overall heat transfer coefficient for the cross-flow region is obtained as

$$UA_{cr} = \frac{2 * N_{plates}}{\left\{\frac{1}{\eta_{oH} A_{tH} h_H} + \frac{t_w}{k_w A} + \frac{1}{\eta_{oC} A_{tC} h_C}\right\}} \tag{A12}$$

Upon determination of the cold side inlet temperature from Eq. A7, the hot side energy balance, assuming no heat loss, is used to determine the hot side exit temperature, T_{ho}

$$\dot{q}_{cr} = C_h(T_{ho} - T_{hi}) \tag{A13}$$

The determined temperatures from Eqs. A7 and A13 and are compared against the original guesses and the iterative procedure continues until convergence.

A3. Nusselt Number and Friction Factor Correlations

Molten salt side:

The molten salt side is represented by straight, rectangular channels. The widely used Moody diagram (Moody (1944)) describes the pressure drop for flows through pipes for a relative roughness of <5 %. However, the roughness of AM microchannels exceeds this limit and modified relations are needed. To take the roughness effect into account for the laminar region Kandlikar et al. (2005) suggested to adjust the hydraulic diameter D_h depending on the roughness. By subtracting the peak to valley roughness, R_z, from D_h, the reduced flow passage is represented. For the turbulent region Kandlikar et al. (2005) replaced the roughness parameter with R_z in the traditional friction factor relation (Miller (1996)). In the turbulent regime, Stimpson et al. (2017) developed another

approach to describe rough surfaces based on a modification of the Moody relative roughness correlation.

To encounter the roughness effect on the friction factor f in the model, the following correlations from Kandlikar et al. (2005) were used for the laminar flow regime,

$$f_H = \frac{24}{Re_H}(1 - 1.355\alpha_H + 1.947{\alpha_H}^2 - 1.790{\alpha_H}^3 + 0.956{\alpha_H}^4 - 0.255{\alpha_H}^5), \quad Re_H < 350 \tag{A14}$$

$$f_H = \frac{1}{16}\left[ln\left(\frac{R_z}{3.7 \times D_H} + \frac{5.74}{{Re_H}^{0.9}}\right)\right]^{-2}, \quad Re_H > 350 \tag{A15}$$

In Equation A14, the aspect ratio α is the minimum over maximum dimension of the duct. The hot side Reynolds number in Eq. A15 was estimated as,

$$Re_H = \frac{\rho_H v_H D_{H,corr}}{\mu_H} \tag{A16}$$

where $D_{H,corr}$ is the corrected hydraulic diameter estimated as

$$D_{H,corr} = D_H - 2 \cdot Rz \tag{A17}$$

by subtracting the peak-to-valley roughness Rz of the channel from the nominal hydraulic diameter, D_H,

$$D_H = 2\frac{W_H H_H}{W_H + H_H} \tag{A18}$$

The pressure drop was estimated from the friction factor as

$$\Delta P_H = 4f_H \times \frac{L}{D_H} \times \frac{\rho_H {v_H}^2}{2} \tag{A19}$$

For Nusselt number of hot side, Gnielinski's correlation and Shah's correlation are used to describe fully developed turbulent flow and laminar flow respectively (Nellis and Klein (2009)),

$$Nu_H = \begin{cases} \dfrac{\frac{f_H}{8}(Re_H - 1000)Pr_H}{1 + 12.7\left({Pr_H}^{\frac{2}{3}} - 1\right)\sqrt{\frac{f_H}{8}}}, & 2300 < Re_H < 5 \times 10^6 \; and \; 0.5 < Pr_H < 2000 \\ 7.54(1 - 2.61\alpha_H + 4.97{\alpha_H}^2 - 5.119{\alpha_H}^3 + 2.702{\alpha_H}^4 - 0.548{\alpha_H}^5), & otherwise \end{cases} \tag{A20}$$

sCO2 side:

Several correlations are found in literature on friction factor and Nusselt number for flow through an array of pin fins; several of these were considered, and the most promising ones are listed in Table A1 for friction factor and Table A2 for Nu along with their range of applicability. To determine which of the correlations best predict the pressure drop and heat transfer, conjugate CFD analyses on a 10 cm unit strip of the pin array were performed with sCO_2 as the working fluid. By virtue of symmetry, to reduce the computational time, only a representative stripe of the heat sink was modeled in the simulations rather than the entire core. Temperature-dependent properties of the fluid were used in the simulations and a prescribed heat flux boundary condition was imposed on the bottom wall. These simulations were carried out for various flow rates corresponding of Reynolds numbers, Re_{Dh} ranging from 1500 to 7000. The pressure drop and average heat transfer coefficient are extracted from the CFD simulation results and compared against the correlations over a range of Re expected in the PHE. The last column in Table A1 and Table A2 report the deviation in terms of the Mean Absolute Deviation, MAD, defined as

$$MAD = \frac{1}{N}\sum_{1}^{N}\frac{|\varphi_{exp} - \varphi_{pred}|}{\varphi_{exp}} \times 100\% \qquad \text{(A21)}$$

Table A1. Selected literature correlations for single-phase friction factors in pin fins arrays

Ref.	Notes	Single phase friction factor correlation	MAD (%)
Prasher et al. (2007)	-Micro pin fin heat sink -Staggered circular and square pin fin	$f = 4 \times 0.295\left(\frac{H}{D_h}\right)^{1.249}\left(\frac{S_L - D_h}{D_h}\right)^{-0.7}\left(\frac{S_T - D_h}{D_h}\right)^{-0.36} Re^{-0.1}$ $Re > 100;\ 1.3 < H_{pin}/D_h < 2.8$ $2 < S_T/D_h < 3.6\ ;\ 2.4 < S_L/D_h < 4$	68.5
Short et al (2002-a)	-Macro pin fin heat sink -Staggered circular pin fin	$f = 4 * 0.221\left(\frac{H}{D_h}\right)^{0.056}\left(\frac{S_L}{D_h}\right)^{-1.4}\left(\frac{S_T}{D_h}\right)^{-0.54} Re^{-0.08}\left(\frac{L}{D_h N_{row}}\right)$ $Re > 1000;\quad 1.9 < H_{pin}/D_h < 7.2$	57.9

		$2 < S_T/D_h < 6.4; \quad 1.8 < S_L/D_h < 3.2$	
Moores and Joshi (2003)	-Meso pin fin heat sink -Staggered circular pin fin	$f = 4 \times 3.2\left(\frac{H}{D_h}\right)^{-0.138} Re^{-0.42}$ $1000 < Re < 10000;\ 0.5 < H_{pin}/D_h < 1.1$ $1.3 < S_T/D_h < 1.36\ ;\ 1.13 < S_L/D_h < 1.18$	36
Zukauskas and Ulinskas (1983)	Tube bank -staggered circular tube -all fluids	$f = 0.343 + 0.303 \times 10^3 Re^{-1} - 0.717 \times 10^5 Re^{-2} + 0.88 \times 10^7 Re^{-3} - 0.38 \times 10^9 Re^{-4}$ $100 < Re < 1E4 \quad S_T/D_h = 2$	29.2

Table A2. Selected literature correlations for single-phase Nusselt number in pin fins arrays

Reference	Notes	Single phase friction factor correlation	MAD%
Rasouli et al. (2017)	-Micro pin fin heat sink -Staggered diamond pin fin	$Nu_{Amin} = 0.039\left(\frac{S_T - D_h}{D_h}\right)^{-0.19} (Re_{Amin})^{0.837} Pr^{0.557}$ $40 < Re_{Amin} < 2300;\ 0.7 < H_{pin}/D_h < 3$ $1.7 < S_T/D_h < 3\ ;\quad 0.8 < S_L/D_h < 1.5$	7.7
Zukauskas (1972)	-Tube bank -Staggered circular tubes -All fluids	$Nu_{Dh} = 0.35\left(\frac{\beta_T}{\beta_L}\right)^{0.2} Re^{0.6} Pr^{0.36} \left(\frac{Pr}{Pr_{wall}}\right)^{0.25}$ $1000 < Re < 2E5$ $\beta_T/\beta_L < 2\ where\ \beta_T = S_T/D_h\ and\ \beta_L = S_L/D_h$	11.9
Short et al. (2002-b)	-Macro pin fin heat sink -Staggered circular pin fin	$Nu_{Dh} = 0.419\left(\frac{H}{D_h}\right)^{-0.3}\left(\frac{S_L}{D_h}\right)^{0.077}\left(\frac{S_T}{D_h}\right)^{0.2} Re^{0.45} Pr^{1/3}$ $Re > 1000; \quad 1.9 < H_{pin}/D_h < 7.2$ $2 < S_T/D_h < 6.4; \quad 1.8 < S_L/D_h < 3.2$	59.4
Prasher et al (2007)	-Micro pin fin heat sink -Staggered circular and square pin fin	$Nu_{Dh} = 0.281\left(\frac{S_L - D_h}{D_h}\right)^{-0.63} Re^{0.73}\left(\frac{Pr_{sCO_2}}{Pr_{water}}\right)^{0.36}$ $Re > 100; \quad 2.48 < H_{pin}/D_h < 2.8$ $2.4 < S_T/D_h = S_L/D_h < 3.6$	221.2 [1]

[1] Re_{Dh} and Re_{Amin} is the Reynolds number based on the regular hydraulic diameter and the hydraulic diameter based on the minimum flow area in the pin array: $Re_{Dh} = \frac{\rho v D_H}{\mu}$ and $Re_{Amin} = \frac{\rho v D_{Amin}}{\mu}$
The Re_{Dh} of 1500 to 7000 plotted corresponds to a 1900-9000 range for Re_{Amin}

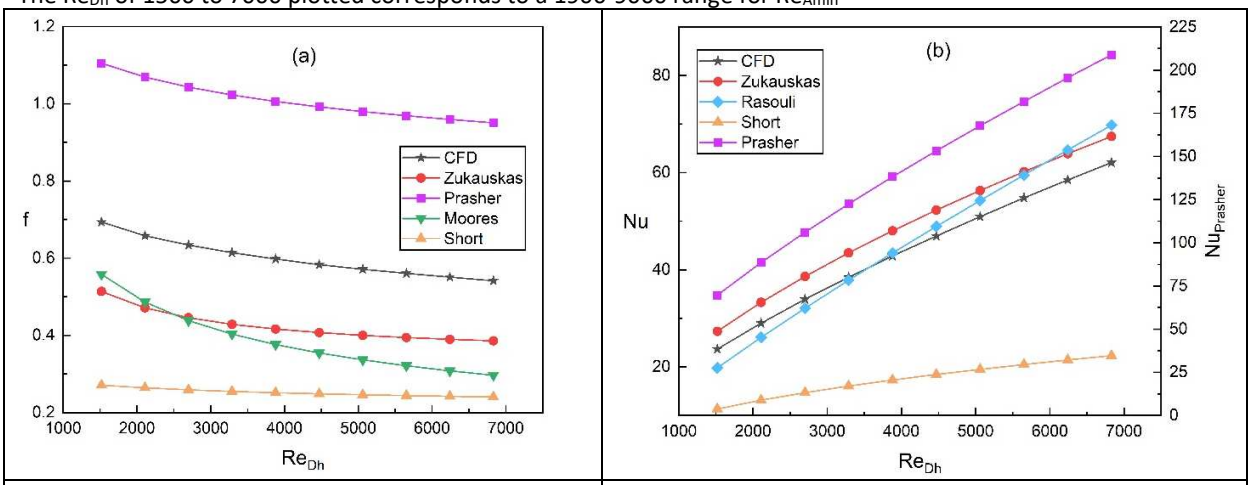

(a) (b)

Figure A1. Comparison of the computed friction factor (a) and Nusselt number (b) with predictions of literature correlations

From Table A1, it is seen that the Zukauskas and Ulinskas (1983) correlation, developed for flow over a bank of tubes, predicts the CFD simulation results with the lowest MAD of 29.2 %. For heat transfer, as seen in Table A2, the Rasouli et al. (2017) correlation predicts the Nu to within 7.7 % of the CFD results, despite falling out of its applicability range. To further explore the prediction trends over the Re range, the CFD and correlation results of friction factor and Nu are compared in Figures A1a and b, respectively.

Comparing the correlations predictions with friction factor derived from CFD, it is seen from Figure A1a that most correlations do not give an accurate estimation of the trend and magnitude of friction factor. The estimates using Prasher et al. (2007) and Short et al. (2002-a) for friction factor deviate significantly because the PHE pin array design falls outside the range of applicability of these correlations for one or more key geometric parameters. The Moores and Joshi (2003) correlation appears to perform slightly better than the Zukauskas and Ulinskas (1983) correlations for the lowest below Re of 2000, but the latter is more consistent and accurately captures the trend observed with the CFD results over all Re. Hence, this correlation is used in the PHE core model. However, it should be noted that the Zukauskas and Ulinskas (1983) correlation results in a 29 percent underprediction of the friction factor. However, given that the pressure drop is very low in the 24 cm and 80-cm PHE designs (see Table 5), even after considering this underprediction, the pressure drop is less than 0.25% of the line pressure.

Comparing the correlations predictions with Nu derived from CFD (Figure A1b), it is seen that Short et al. (2002-b) and Prasher et al. (2007) significantly underpredict and overpredict the CFD results, respectively. The Rasouli et al. (2017) and Zukauskas (1972) correlations both provide low MAD predictions of the heat transfer, with Zukauskas accurately capturing the trend of Nusselt numbers displayed by the CFD simulations, while consistently overpredicting the CFD results. Based on the lower MAD over the Re range anticipated in the PHE, the Rasouli et al. (2017) correlation was selected for the PHE core model.

With respect to incorporation of surface roughness effects on pressure drop on the sCO_2 side, correlations in literature of flow and heat transfer through a pin array do not account for surface roughness effects. As a starting point, Kandlikar et al.'s (2005) modification to the channel dimension (Eq. A17) was used to incorporate surface roughness effects on the pin array side as well. Further work is needed to characterize the effect of surface roughness on pin array pressure drop and heat transfer rate.

The pressure drop in the counter-flow section was modeled using the correlation for staggered pin array arrangement of Zukauskas and Ulinskas (1983); however, due to the different flow direction in this section, an in-line correlation by the same authors was selected. Two exponents in the in-line correlation were obtained by digitizing the accompanying plot of friction factor as a function of Reynolds number.

A4. Thermofluidic Core Model Cross-flow Calibration

The actual PHE geometry includes a cross flow section, a counter-flow region, but also a hybrid zone that is neither cross nor counter-flow. In order to obtain a model which reflects this combination in the evaluated performance, a calibration step is added to the procedure and CFD simulations for the unit-cell core consisting of half-height plate, analogous to that performed for the plate flow uniformity study is used to determine a calibration factor F_{corr} to the cross-flow effectiveness in Equation A7.

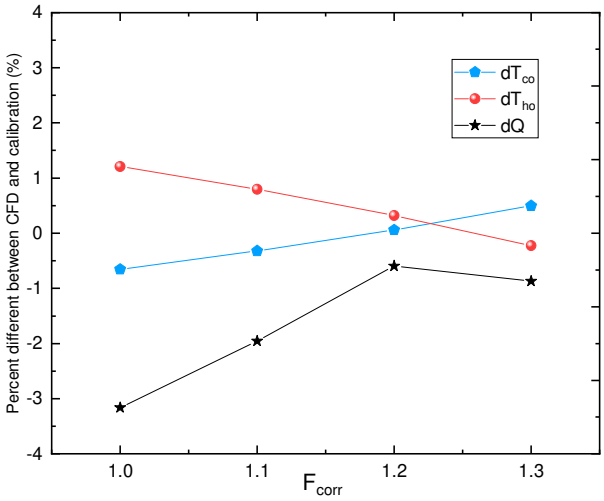

Figure A2. Percent difference between CFD simulation of unit-cell core and thermofluidic model predictions as a function of the calibration factor F_{corr}

Table A3. Correlation-based model calibration

ε increase (%)	T_co (C)	T_ho (C)	dP_c (Pa)	% diff T_co	%diff T_ho	%diff dP	Q (W)	% diff Q
0	695.6	530.8	331.3	-0.656	1.209	-24.089	12201	-3.162
10	698.0	528.6	332.2	-0.322	0.796	-23.822	12350	-1.954
20	700.6	526.1	333.3	0.058	0.321	-23.491	12519	-0.595
30	703.7	523.2	334.7	0.496	-0.224	-23.063	12484	-0.870
CFD	700.2	524.4	422.0	-	-	-	12593	-

Table A3 shows the exit temperature on both sides and pressure drop on the cold side as a function of the percent increase in F_{corr} with 1 corresponding to 100% cross-flow and followed by the efficiency increasing in 10% increments. As expected, the comparison between CFD simulation and model is observed to improve with the efficiency. A F_{corr} of 1.2 was selected as final configuration and a good agreement is noted between the model and the CFD temperatures with a 0.06% and 0.32% difference between the CFD and Matlab sCO_2 and MS outlet temperatures, respectively. As shown in Figure A2, a F_{corr} of 1.2 minimizes the relevant parameters taken as a whole. The difference observed even after calibration is likely due to the uniqueness of the PHE design that forces the flow to redirect at an angle.

For the pressure drop however, a 23.5% difference mismatch is observed with the Zukauskas and Ulinskas (1983) correlation prediction. This result is consistent with results of the counter-flow stripe section (Figure A1a and Table A1), which showed that the correlation underpredicts the CFD pressure drop.

An Additively-Manufactured Primary Heat Exchanger For Solar Thermal Power Generation

Mechanical and Thermo-fluidic design

- Mechanical and CFD simulations
- correlation-based thermofluidic model of core

Metal Additive Manufacturing

- Porosity-process parameter map
- Surface roughness
- Core geometry dimensional tolerance

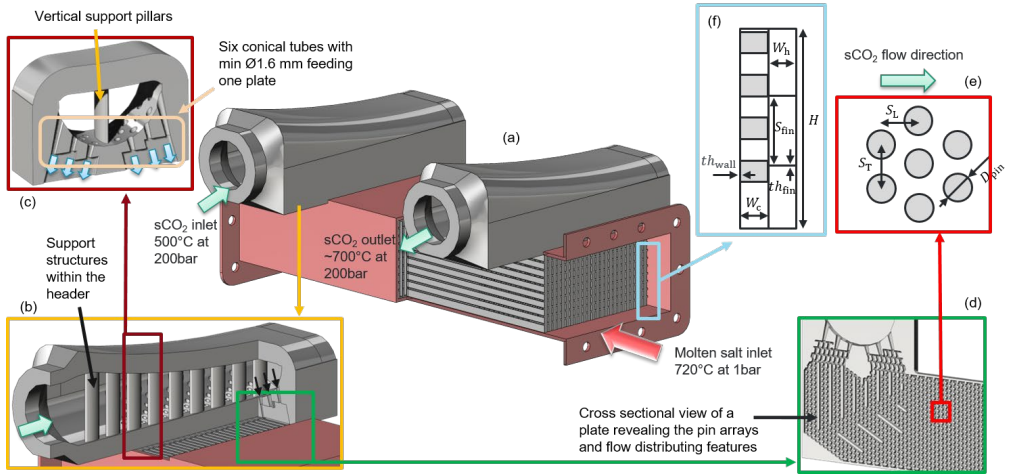

Process Based Cost Model